Biomedicine & Pharmacotherapy 195 (2026) 118950

Contents lists available at ScienceDirect

Biomedicine & Pharmacotherapy

journal homepage: www.elsevier.com/locate/biopha

Safety of ferrite nanoparticles for biomedical applications: Cyto- and genotoxic effects of $M_xFe_{3-x}O_4$ (M = Fe, Zn, Mn) in an Advanced 3D human hepatic *in vitro* model

Iza Rozman [a,b], Alvaro Gallo-Cordova [c], María del Puerto Morales [c], Marco A. Morales Ovalle [d], Gerardo F. Goya [e], Katja Kološa [a], Domen Hočevar [b], Bojana Žegura [a,b,*,1], Alja Štern [a,b,*,1]

[a] National Institute of Biology, Department of Genetic Toxicology and Cancer Biology, Večna pot 121, Ljubljana, Slovenia
[b] Biotechnical Faculty, University of Ljubljana, Jamnikarjeva ulica 101, Ljubljana, Slovenia
[c] Instituto de Ciencia de Materiales de Madrid, ICMM-CSIC, C Sor Juana Inés de la Cruz 3, Madrid 28049, Spain
[d] Instituto de Nanociencia y Nanotecnología, CNEA, CONICET, Centro Atómico Bariloche, Av. Bustillo 9500, SC de Bariloche 8400, Argentina
[e] Institute of Nanoscience and Materials of Aragón (INMA), CSIC-, University of Zaragoza, 12, C. de Pedro Cerbuna, Zaragoza 50009, Spain

ARTICLE INFO

Keywords:
DNA damage
Genotoxicity
HepG2 spheroids
Magnetic ferrite-based nanoparticles
ROS induction
Safety assessment
Toxicogenomics

ABSTRACT

Given the growing interest in nanosized spinel-type ferrite nanoparticles for biomedical applications and the limited information on their safety, this study aimed to assess their cellular and genotoxic effects in an *in vitro* 3D human hepatic cell model (HepG2 spheroids). Ferrite nanoparticles – γFe_2O_3 (FeNPs; 14 ± 4 nm), $Zn_{0.7}Fe_{2.3}O_4$ (ZnNPs; 14 ± 5 nm), and $Mn_{0.4}Fe_{2.6}O_4$ (MnNPs; 7 ± 2 nm) – were synthesised through a microwave-assisted polyol route, functionalized with citric acid, and characterised using Inductively Coupled Plasma Optical Emission Spectroscopy (ICP-OES), Transmission Electron Microscopy (TEM), X-ray Diffraction (XRD), and Fourier Transform Infrared Spectroscopy (FTIR). Nanoparticle uptake was analysed using TEM, cytotoxicity was measured with CellTiter-Glo®, and oxidative stress induction was assessed using the 2′,7′-Dichlorodihydrofluorescein diacetate (DCFH-DA) and malondialdehyde (MDA) assay. Genotoxic effects were evaluated using the comet, γH2AX and p-H3 assays. Cellular stress responses were assessed using toxicogenomic analysis. Significant cytotoxicity of the tested nanoparticles (0.1–250 μg/mL) was observed; however, TEM analysis revealed limited penetration to the outermost cell layers of spheroids. Notably, only FeNPs induced ROS generation, while MDA levels remained unchanged in all tested samples. Low DNA damage was detected at 24 h, but a significant increase was observed at 96 h (5–50 μg/mL). No increase in γH2AX or p-H3 was found. No substantial alterations in DNA damage or oxidative stress-response gene expression were detected. Altogether, our findings suggest that the effects of ferrite nanoparticles are time- and composition-dependent, underlining the importance of further mechanistic and chronic exposure evaluations in 3D cell models.

1. Introduction

Nanosized spinel-type ferrites, a novel class of engineered nanomaterials, have attracted considerable interest among researchers in various fields, including physics, chemistry, biology, medicine, materials science, and engineering [1–3]. While they have proven to be valuable and interesting in both their practical applications and fundamental scientific significance, due to their unique and remarkable tunable physicochemical properties, the aspect of their safety is often overlooked.

Ferrites are a broad class of ceramic ferrimagnetic materials with the general formula $M_xFe_yO_z$, where M denotes a divalent cation from transition metals. Iron oxides such as magnetite (Fe_3O_4) and maghemite (γFe_2O_3) are ferrites composed only of iron cations; however, the term "ferrite" often refers to doped or mixed-metal ferrites in which Fe_2O_3 is combined with other metal ions [4]. This compositional tunability

* Corresponding authors at: National Institute of Biology, Department of Genetic Toxicology and Cancer Biology, Večna pot 121, Ljubljana, Slovenia.
E-mail addresses: bojana.zegura@nib.si (B. Žegura), alja.stern@nib.si (A. Štern).
[1] These authors contributed equally to this work

https://doi.org/10.1016/j.biopha.2025.118950
Received 10 November 2025; Received in revised form 17 December 2025; Accepted 27 December 2025
Available online 6 January 2026

allows precise control over magnetic, electrical, and structural properties. Common dopants include cobalt, manganese, magnesium, nickel, zinc, copper, and silver, which can significantly enhance performance and stability depending on the targeted application [3, 5–7].

Since Fe, Zn, and Mn are involved in many biological processes [8], it is assumed that they can be safely incorporated into the labile pools of all three elements [9–11] and thus ferrite nanoparticles (NP) containing Zn and Mn are widely exploited. Manganese ferrite NP exhibit notable advantages over others because of their high catalytic activity, easy synthesis, and simple modifications. They are considered environmentally friendly and can be separated from the reaction medium, utilising their magnetic properties [12]. Zinc ferrite NP have attracted considerable attention as well, due to their valuable electrical, dielectric, chemical, optical, and especially magnetic properties [13]. Namely, their distinctive magnetic properties are due to the non-magnetic nature of the zinc atom; thus, their modification and improvement are possible simply by tuning the chemical position of the NP [14].

Publications related to the synthesis and application of various ferrite NP, including zinc and manganese ferrite NP, have increased tremendously in the last few years [4]. Yet, the potential use of zinc and manganese ferrite NP in biomedicine applications requires an in-depth study of the possible toxicity induced by NP administration. Previous studies have reported decreased cell viability in MCF-7 cells [15], cytotoxicity, and oxidative stress in different human cell models *in vitro* [16], progressive increase of apoptotic and necrotic activity in 4T1 cells [17], and, on the other hand, non-toxic effects in human breast cancer (MDA-MB-23) and human prostate cancer (PC-3) cells [18]. Nevertheless, the lack of consensus in the experimental conditions, including methods, materials, and cell models used, makes it difficult to obtain holistic conclusions, especially when it comes to genotoxicity. Only a few studies on ferrite NP genotoxicity can be found in the literature. Abudayyak et al. (2017) [19] reported that cobalt ferrite NPs do not induce DNA damage in NRK-52E kidney cells (up to 100 μg/mL). Still, they observed a significant decrease in cell viability due to the induction of apoptosis/necrosis at 100 μg/mL. Sanz-Sagué et al. (2024) [20] showed that vanadium spinel ferrite NPs cause low genotoxicity and cytotoxicity in HepG2 cells (up to 100 $\mu g/cm^2$); nevertheless, no influence on the cellular genomic integrity was reported [21].

Overall, the importance of conducting comprehensive safety assessments of ferrite NPs in preclinical studies has been significantly overlooked. Our study aims to fill this critical knowledge gap by evaluating the cyto- and genotoxic potential of three metal ferrite nanoparticles (MNPs) – citric-coated γFe_2O_3, $Zn_{0.7}Fe_{2.3}O_4$, and $Mn_{0.4}Fe_{2.6}O_4$ – *in vitro*, thereby contributing to a clearer understanding of their safety for biomedical applications, such as targeted drug delivery, imaging systems and/or magnetic hyperthermia [22].

The studied MNPs were prepared through a sustainable and scalable microwave-assisted polyol method and functionalised with citric acid for colloidal stability. For the toxicological assessment, an advanced 3D cell model, spheroids prepared from human hepatocellular carcinoma (HepG2) cells, was applied for the first time, offering increased validity and predictivity for human exposure.

The cytotoxicity of the tested MNPs was evaluated using a luminescent assay, measuring ATP, and the generation of reactive oxygen species (ROS) was measured using the DCFH-DA probe. Additionally, the malondialdehyde (MDA) assay was performed to evaluate lipid peroxidation. Genotoxic potential was assessed through the alkaline comet assay and by flow cytometry analysis of γH2AX and p-H3 as genotoxicity biomarkers. A toxicogenomics approach based on targeted gene expression analysis was applied to evaluate the stress response of cells exposed to the MNPs.

Our findings will substantially advance our understanding of ferrite-type NP safety, bringing us one step closer to minimizing potential risks to human health.

2. Materials and methods

2.1. Synthesis of ferrite nanoparticles

Metal ferrite NP $M_XFe_{3-X}O_4$ (M = Fe, Mn, Zn), hereinafter referred to as MNPs, were synthesised via a microwave-assisted polyol route [23] using a Monowave 300® reactor (Anton Paar GmbH, Graz, Austria) operating at 2.45 GHz. In a typical synthesis, 1.73 mmol of iron(II) acetate was dissolved in 19 mL of a solvent mixture composed of 96.3 % diethylene glycol (DEG) and 3.7 % deionised water (v/v), contained in a 30 mL borosilicate glass vial equipped with a magnetic stir bar. For doped samples, manganese(II) acetate or zinc(II) acetate was added to the reaction mixture to achieve a Fe:M molar ratio of 2:1, where M represents either Mn or Zn. The reaction suspension was stirred at 600 rpm and heated at a rate of 3.75 °C per minute until reaching 170 °C, which was maintained for 2 h before rapidly cooling to 55 °C. The resulting dispersion was centrifuged at 8000 rpm for 45 min, and the recovered solid was washed three times with ethanol (15 min each, 8000 rpm). The purified NP were dried under ambient air flow and redispersed in distilled water. The undoped ferrite sample was further subjected to acidic treatment following a previously reported protocol to improve colloidal stability by fully oxidising the sample [24].

All MNPs were then functionalised with citric acid to improve colloidal stability. For the coating process, 200 mg of citric acid was dissolved in 30 mL of deionised water, and the pH was adjusted to 4.0 using 5 M KOH. Then, 20 mL of NP suspension (at a concentration of 5 mg/mL) was added to the solution under continuous mechanical stirring. The mixture was heated to 80 °C and maintained at that temperature for 1 h to facilitate citrate adsorption onto the NP surface. The resulting citrate-coated NP were recovered by centrifugation, washed with ethanol to remove unbound citrate, and redispersed in water.

2.2. Nanoparticles characterisation

The elemental composition of the MNPs was determined by inductively coupled plasma optical emission spectroscopy (ICP-OES) using a PerkinElmer OPTIMA 2100DV system (Waltham, MA, USA). Before analysis, the samples were subjected to acid digestion in aqua regia (HCl: HNO_3, 3:1 v/v) at 90 °C for 12 h to ensure complete dissolution of the metal oxides. The resulting solutions were then analysed to quantify iron and dopant (Zn or Mn) concentrations, allowing the calculation of the actual stoichiometry of each sample.

The structural and morphological features of the MNPs were characterised by transmission electron microscopy (TEM), employing a JEOL JEM 1010 (JEOL Ltd., Tokyo, Japan) operating at an acceleration voltage of 100 kV. For analysis, aqueous suspensions of the NP were drop-cast onto copper grids coated with amorphous carbon and allowed to air-dry at ambient temperature. Particle size distributions were obtained by measuring approximately 200 individual particles per sample on representative TEM micrographs using ImageJ software, considering their longest internal axis. Crystalline phase identification and structural analysis were performed by X-ray diffraction (XRD) using a Bruker D8 Advance (Bruker AXS GmbH, Karlsruhe, Germany) diffractometer equipped with a CuKα radiation source. Diffractograms were recorded in the 2θ range of 20° to 70°, and the average crystallite size was calculated from the [311] reflection using the Scherrer equation, based on the peak's full width at half maximum (FWHM). To confirm the presence of the coating, FTIR spectra in the range of 250 – 4000 cm^{-1} were obtained using a Bruker IFS 66VS. The samples were prepared by pressing into pellets a mixture of dried powder in KBr at 2 % w/w.

To assess the colloidal stability of the MNPs, dynamic light scattering (DLS) measurements were conducted using a Zetasizer Nano SZ (Malvern Instruments Ltd., UK) equipped with a 633 nm He-Ne laser. Hydrodynamic diameters were recorded using water as dispersant at neutral pH, with size values reported based on intensity-weighted distributions.

2.3. Cell cultivation, spheroid preparation, and exposure to MNPs

The human hepatocellular carcinoma-derived cell line HepG2 (ATCC-HB-8065™, Manassas, VA, USA) was cultivated in MEM medium (MEM-10370–046) supplemented with 10 % FBS, all from Gibco (Paisley, Scotland, UK) and 1 mM sodium pyruvate, 2 mM L-glutamine, 100 IU/mL penicillin/streptomycin, and NEAA, all from Sigma-Aldrich (St. Louis, MO, USA), at 37 °C in a humidified atmosphere with 5 % CO_2. Cell passages between 3 and 13 were used to prepare spheroids using the force floating method as previously described by Štampar et al. [25]. Briefly, cells were seeded onto 96-well U-bottom plates (Corning Costar Corporation, New York, USA) at 3,000 cells/well in complete cell growth medium containing 4 % methylcellulose. The plates were centrifuged at 900 × g for 90 min, and the formed spheroids were left to mature for 72 h before the experiments, at 37 °C and 5 % CO_2.

For the experiments, three-day-old HepG2 spheroids were exposed to graded concentrations of MNPs for 24 and 96 h. For the cytotoxicity experiments, spheroids were exposed to MNP concentrations in the range of 0.1–250 μg/mL, corresponding to 0.04–100 μg/cm^2. Tested concentrations were determined based on the OECD Test Guideline No. 487, adapted by Michael J Burgum et. al. (2024) [26]. For all subsequent experiments, noncytotoxic concentrations in the range of 5–50 μg/mL, corresponding to 2–20 μg/cm^2, were evaluated.

A negative (cell medium), a vehicle (up to 3.12 % MiliQ water), and assay-specific positive controls were included in all experiments. For the NP internalisation experiments, the spheroids were exposed to the MNPs at a concentration of 50 μg/mL.

2.4. Analysis of nanoparticle distribution in spheroids – transmission electron microscopy (TEM)

To assess the spatial distribution of MNPs within the 3D cellular architecture of HepG2 spheroids, TEM analysis was performed after 24 and 96 h of exposure. HepG2 spheroids were prepared as described above and incubated with each NP type at a concentration of 50 μg/mL. Following incubation, spheroids were collected, gently washed with phosphate-buffered saline (PBS, pH 7.4) to remove unbound NP, and fixed in 2 % glutaraldehyde in 0.1 M phosphate buffer (PB, pH 7.2) for 2 h at room temperature, followed by incubation in 1.5 % glutaraldehyde in 0.05 M PB at 4°C overnight. Post-fixation was carried out with 1 % osmium tetroxide for 1 h at room temperature, followed by dehydration through a graded ethanol series (30 %, 50 %, 70 %, 90 %, and absolute ethanol) and infiltration with epoxy resin. For cross-sectional analysis, resin-embedded spheroids were polymerised at 60 °C for 48 h, and ultrathin sections (~70 nm) were obtained using an ultramicrotome. Sections were collected on copper grids and stained with uranyl acetate (2 % aqueous) and lead citrate to enhance contrast. Imaging was performed using a Tecnai T20 transmission electron microscope (Thermo Fisher Scientific, USA) operated at 200 kV. For each sample and time point, at least three spheroids were analysed. Additionally, in one selected spheroid, a systematic series of TEM images was acquired along a straight linear trajectory across the section, beginning at one external edge of the spheroid and progressing through consecutive adjacent fields until reaching the opposite border, and then the images were composed into a single frame.

2.5. Cytotoxicity – measurement of the ATP content

After the exposure, cytotoxicity of MNPs was evaluated with the CellTiter-Glo® Luminescent Cell Viability Assay (Promega, Madison, WI, USA), a method to determine the number of viable cells based on luminometric quantitation of ATP. The assay was performed according to the manufacturer's instructions with minor modifications. Shortly, the spheroids in 50 μL of cell media were transferred to a white-opaque 96-well plate (Thermo Scientific™, Waltham, MA, USA), and 50 μL of the assay reagent was added to each well. The content of each well was resuspended by pipetting to ensure complete lysis of cells in the spheroid, and the reaction was incubated for 20 min at room temperature altogether. The luminescence was measured using a luminometer (Sinergy MX, BioTek, Winooski, VT, USA). The experiment was performed in five replicates per experimental point and repeated three times independently. DMSO (23 % for 24 and 5 % for 96 h) was used as the positive control (PC). Half-maximal inhibitory concentrations (IC_{50}) and concentrations reducing cell viability to 70 % (IC_{30}) were calculated using the GraphPad Prism v10 software (GraphPad Software, San Diego, CA, USA), using a nonparametric local regression method (LOWESS), which fits a smoothed curve to the dose–response data without assuming a predefined model.

2.6. Generation of reactive oxygen species (ROS) – DCFH-DA probe

To measure the generation of ROS in HepG2 spheroids after exposure to MNPs, we used the probe DCFH-DA (Abcam, Cambridge, UK), which has excitation and emission wavelengths of 498 nm and 522 nm, respectively. Before MNPs exposure, spheroids were treated with a DCFH-DA probe for 30 min. After that, the probe was removed, and spheroids were washed with 1x PBS. HepG2 spheroids were then exposed to graded concentrations of MNPs prepared in Hank's Buffered Salt Solution (HBSS, Merck, Darmstadt, Germany) for 2 and 4 h. The fluorescence was detected with an excitation wavelength of 485 nm and an emission wavelength of 530 nm at each time point using a BioTek Cytation 5 Cell Imaging Multimode Reader (Agilent, Santa Clara, USA). The experiment was performed in five replicates per experimental point and repeated three times independently. 1 mM tBHP was included as a positive control.

2.7. Lipid peroxidation – MDA assay

Lipid peroxidation as a valuable marker for oxidative stress and cellular damage was measured using the Lipid Peroxidation (MDA) Assay Kit (Abcam, Cambridge, UK). Lipid peroxidation is determined by the reaction of MDA (malondialdehyde) with thiobarbituric acid (TBA) to form a colourimetric/fluorometric product proportional to the MDA present in the sample. After exposure, the spheroids were collected, washed with 1x PBS at each exposure time point, and homogenised using MDA Lysis Buffer supplemented with butylated hydroxytoluene (BHT). Homogenised samples were then centrifuged at 13000 × g for 10 min, and the supernatant was placed into a microcentrifuge tube containing TBA solution, prepared as described by the manufacturer. Samples were then incubated at 95 °C for 60 min and cooled down for 10 min in an ice bath. Fluorescence was measured at Ex/Em 531/590 nm using the BioTek Cytation 5. The experiment was performed in three replicates per experimental point and repeated three times independently. A positive control (1 mM tBHP, 3-hour exposure) was included in the experiments.

2.8. The alkaline comet assay

After exposure to MNPs, DNA damage induction was studied using the alkaline comet assay. After 24 and 96 h of exposure, spheroids were dissociated into a single-cell suspension by collagenase treatment. The comet assay was conducted as described by Štampar et. al. [27] under conditions described in the Supplement material (Table S1). For comet scoring, slides were stained using the GelRed nucleic acid stain (Biotium, USA) according to the manufacturer's instructions. Analysis and scoring were performed using a fluorescent microscope and Comet Assay IV software (Instem, Philadelphia, USA). The percentage of DNA in the tail (% tail DNA) of the comet was evaluated. A positive (30 and 5 μM benzo [*a*]pyrene; BaP for 24 and 96 h, respectively) control was included. Each experiment was conducted independently three times, analysing 50 nuclei per experimental point.

2.9. Analysis of γH2AX and p-H3 positive cells by flow cytometry

The phosphorylation of the histones H2AX (γH2AX) and H3 (p-H3), which are biomarkers for the induction of DNA double-strand breaks (DSBs) - clastogenic effects – and mitotic disturbance – aneugenic effects, respectively, was evaluated by flow cytometry. After exposure, the spheroids were dissociated to a single-cell suspension, washed twice with 1x PBS, fixed with 4 % formaldehyde (PFA), and stored at 4 °C. For immunolabeling, cells were washed with 1x PBS and incubated for 30 min in 1 % BSA with 50-fold diluted antibodies against γH2AX pSer139-APC [130–123–256] and pH3-PE [130–105–700] or REA Control (I)-APC [130–120–709] and REA Control (I)-PE [130–104–613] to discriminate unspecific binding of antibodies. As positive controls (PC), spheroids exposed to etoposide (1.7 μM) and colchicine (0.1 μM) were used. Samples were analysed using a flow cytometer MACSQuant Analyzer 10 with MACSQuantify™ software (Miltenyi Biotech, Germany) and FlowJo V10 software (Becton Dickinson, New Jersey, USA). Each experiment was carried out independently three times, and 10,000 events were acquired per sample.

2.10. Targeted toxicogenomic analysis

The expression of selected genes after exposure to MNPs was analysed by qPCR primer assays (Applied Biosystems, USA) and One 48.48 Dynamic Array IFC for Gene Expression (Fluidigm, USA). After 24 and 96 h of exposure, the spheroids were collected, and total RNA was isolated using the RNeasy Mini Kit from Qiagen (Qiagen, Germany) according to the manufacturer's instructions. 10 μg/mL etoposide served as the positive control for the toxicogenomic analysis. The concentration, purity and quality (Figure S2) of the isolated RNA, the reverse transcription (using the Transcription Kit from Applied Biosystems, MA, USA), the preamplification of the selected genes (using the TATAA PreAmp GrandMasterMix from Tataa Biocenter, Gothenburg, Sweden), and the gene expression analysis (using the TaqMan Universal PCR Master Mix and Taqman Gene Expression Assays in Table S2) were performed as described by Štern et. al. [30]. Reaction conditions for toxicogenomic analysis are presented in Table S5, Table S6, and Table S7. Biologically important up- or downregulation was defined as a relative expression change greater than 1.5-fold.

2.11. Statistical analysis

Statistically significant differences between MNPs-exposed cells and the vehicle control groups (VC; up to 3 % MilliQ water in cell media) were analysed using the GraphPad Prism v10 software (GraphPad Software, San Diego, CA, USA). Before statistical analysis, data sets were tested for normality (Shapiro-Wilk for all sample sets and Kolmogorov-Smirnov for flow cytometry data) and heteroscedasticity (Spearman's test). One-way analysis of Variance (ANOVA) and Dunn's or Dunnett's multiple comparison test were used for the analysis of the data generated in the CellTiter-GLO®, DCFH-DA, γH2AX, and p-H3 assays. The Kruskal–Wallis nonparametric test and Dunn's multiple comparison test were used for the comet assay data analysis. Two-way ANOVA followed by Šídák's multiple comparisons test and Fisher's LSD test were used for the analysis of the MDA assay and toxicogenomic analysis, respectively.

3. Results & discussion

Magnetic nanoparticles (MNPs) are widely used across industries, including pharmaceuticals, food, agriculture, cosmetics, electronics, construction, and packaging. Their growing utilisation is driven not only by their versatile properties but also by the expanding recognition of their potential in biomedical applications. Notably, MNPs are being explored for targeted drug delivery [31–33], cancer therapy [34–39], wound healing [40], and treatment of Alzheimer's disease [41–44], raising concerns about their potential impact on human health and the environment. To address this need, the present study evaluated the safety of three types of ferrite MNPs using advanced *in vitro* 3D models, providing insight into their potential biological effects.

The microwave-assisted polyol method employed to prepare the MNPs samples offers a sustainable and scalable route for the synthesis of high-quality ferrite NP. It combines the advantages of rapid, energy-efficient heating with precise control over particle size and crystallinity, while significantly shortening reaction times and reducing energy consumption [45]. Given the increasing use of this method for biomedical nanomaterial production, a thorough toxicological assessment of the resulting NP is essential to ensure their safe application.

In the present study, the toxicological effects of MNPs were comprehensively evaluated using an advanced 3D HepG2 spheroid model established using the forced floating method [46]. The HepG2 cell line is widely used in liver toxicity studies and for elucidating toxicity mechanisms [47], as it expresses wild-type p53 [48] and retains the activity of key metabolizing enzymes [49]. The HepG2 cell line serves as a widely adopted *in vitro* model for hepatotoxicity studies, offering advantages such as an unlimited lifespan, stable phenotype, high availability, and ease of handling [50]. Considering that the liver is the main organ for nanoparticle accumulation after entering the body [51], using 3D HepG2 spheroids allows for a physiologically relevant assessment of potential hepatotoxic effects. HepG2 cells are traditionally cultured as monolayers, but under these conditions, they fail to recapitulate the physiological properties of tissues and are limited in their ability to predict *in vivo* responses. In the present study, we therefore employed a 3D cell model (spheroids), in which cells are surrounded by a natural extracellular matrix (ECM). This arrangement promotes tissue-specific architecture, facilitates direct cell–cell and cell–ECM interactions, and provides a more physiologically relevant, *in vivo*-like environment. Additionally, spheroids exhibit enhanced stability, maintaining high cell viability and morphology over several weeks, which allows for prolonged exposure studies [52]. Cytotoxicity of the MNPs was assessed by measuring luminescence, while genotoxicity was evaluated through several endpoints, including cell proliferation, DNA damage, genomic instability, and gene expression.

3.1. Nanoparticles characterisation

The elemental composition determined by ICP-OES was used to calculate the actual stoichiometry of the doped ferrites, yielding $Zn_{0.7}Fe_{2.3}O_4$ for ZnNPs and $Mn_{0.4}Fe_{2.6}O_4$ for MnNPs, confirming the effective incorporation of the dopants into the spinel structure and enabling a detailed comparison of their structural and colloidal properties. Fig. 1 illustrates these differences across all samples. TEM micrographs (Fig. 1A) revealed that FeNPs, ZnNPs and MnNPs consisted of predominantly quasi-spherical to slightly faceted particles, with no elongated or plate-like morphologies observed. Particle size histograms (Fig. 1B) showed that FeNPs and ZnNPs exhibited similar average particle sizes (~14 nm), while MnNPs consisted of significantly smaller NP (7 ± 2 nm), indicating a larger surface-to-volume ratio. X-ray diffraction (Fig. 1C) revealed that the crystallite sizes of FeNPs and ZnNPs were also ~13–14 nm, whereas MnNPs displayed a much smaller crystallite size of 7 nm. The close match between particle and crystallite size suggests that these particles are predominantly monocrystalline. Notably, only the Mn-doped ferrite (MnNPs) exhibited a pronounced reduction in particle size, likely due to its lower ionic radius and weaker metal–oxygen bond strength compared to iron, promoting rapid nucleation and limiting crystal growth. Conversely, Zn^{2+}, with its larger ionic radius and preference for tetrahedral sites, tends to induce surface enrichment and lattice distortion, stabilising larger crystallites and even promoting particle coarsening. The presence of Zn at the particle surface, as reported in related XPS studies, may also passivate active growth sites, thereby altering the crystallisation pathway and limiting size confinement [53]. These structural differences were further reflected in the lattice parameters. FeNPs, composed of pure maghemite, displayed a

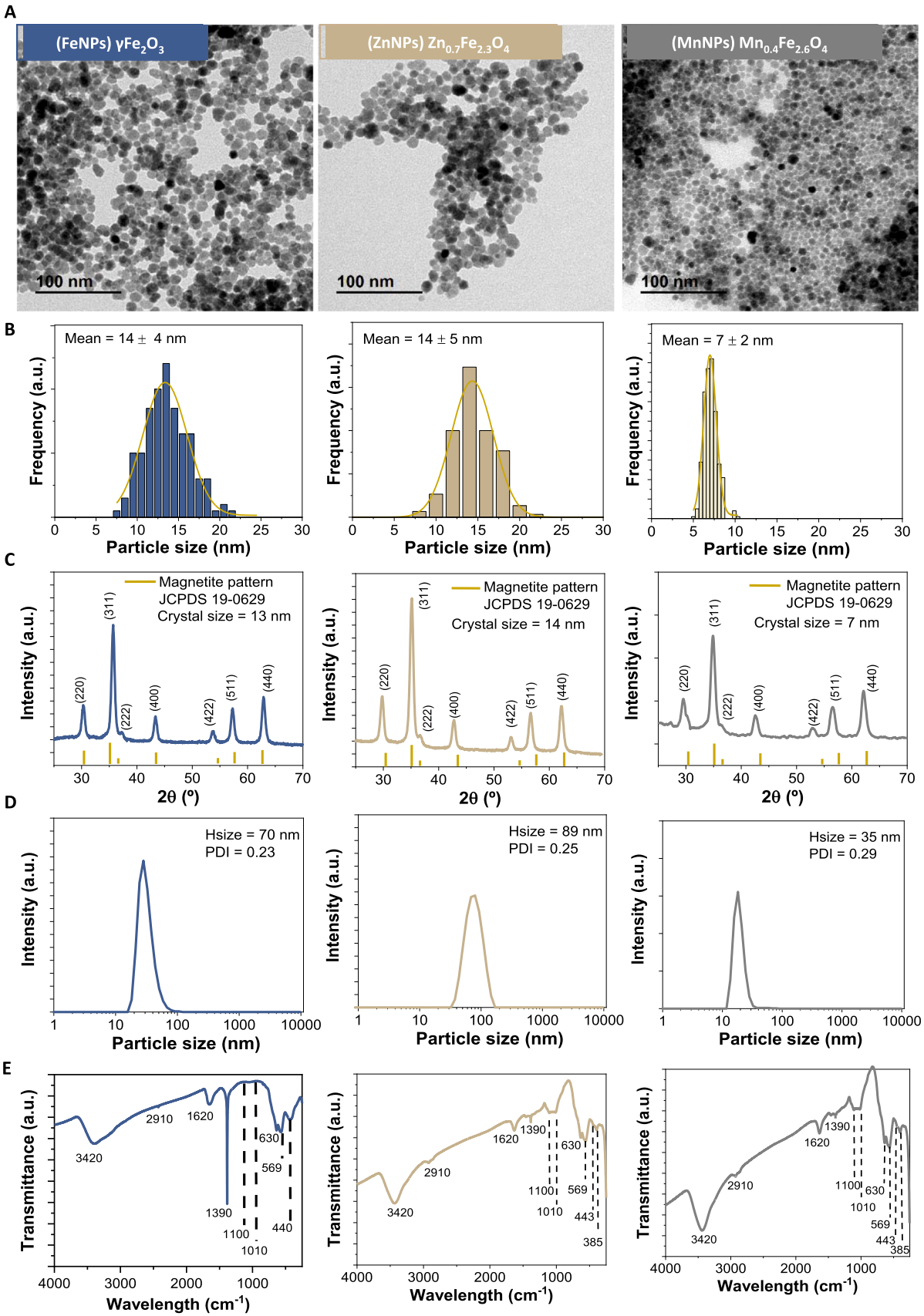

Fig. 1. Characterisation of ferrite samples: γFe_2O_3 (FeNPs), $Zn_{0.7}Fe_{2.3}O_4$ (ZnNPs), $Mn_{0.4}Fe_{2.6}O_4$ (MnNPs). A) Transmission electron microscopy (TEM) images showing particle morphology (scale bar = 100 nm). B) Size distribution histograms derived from TEM micrographs (n < 200) fitted with a log-normal function. C) X-ray diffraction (XRD) patterns indexed to the magnetite spinel structure (JCPDS 19–0629), crystal sizes were estimated using the Scherrer equation. D) hydrodynamic size distributions given in intensity (PDI = polydispersity indices). E) Fourier-transform infrared (FTIR) spectra.

lattice parameter of 8.346 ± 0.001 Å, while ZnNPs and MnNPs exhibited expanded unit cells of 8.438 ± 0.037 Å and 8.417 ± 0.043 Å, respectively. The observed expansion is consistent with the partial substitution of Fe^{3+} by Zn^{2+} and Mn^{2+} [54], confirming successful doping and its influence on the crystal structure.

Altogether, between the three formulations, differences in composition and primary particle size, rather than marked changes in morphology, appear to be the key structural factors likely to influence their differential biological behaviour.

Dynamic light scattering (Fig. 1D), on the other hand, provides insight into the colloidal behaviour of the NP in aqueous media. All three samples exhibited hydrodynamic diameters compatible with stable colloidal suspensions, which is attributed to the presence of the citrate coating that enhances negative surface charge and electrostatic repulsion. Although zeta potential was not measured here, citrate-coated ferrite nanoparticles commonly exhibit negative surface potentials at neutral pH (≈ −10 to −40 mV) due to surface carboxylate groups, consistent with previous reports [55,56]. FeNPs and ZnNPs showed hydrodynamic diameters of 70 nm (PDI = 0.23) and 89 nm (PDI = 0.24), respectively, likely reflecting mild aggregation or hydration layers around the citrate-capped surfaces. In contrast, MnNPs presented a notably smaller hydrodynamic diameter (~36 nm) and a slightly broader distribution (PDI = 0.29).

The FTIR spectra (Fig. 1E) of the ferrite NP displayed distinct vibrational features that provide insight into surface chemistry and functionalization. A broad band centred around 3420 cm^{-1} was observed in all samples and was attributed to the O–H stretching vibration of surface-adsorbed water. In contrast, the peak at 2910 cm^{-1} corresponded to the C–H stretching vibration of the citrate coating, accompanied by an additional characteristic band at 1620 cm^{-1} , assigned to asymmetric $–COO^-$ stretching. The FeNPs spectrum (blue line) shows a strong band at 1390 cm^{-1} that can be ascribed to the presence of nitrate residues from the acidic treatment. And finally, the fingerprint region (630–385 cm^{-1}) shows prominent peaks

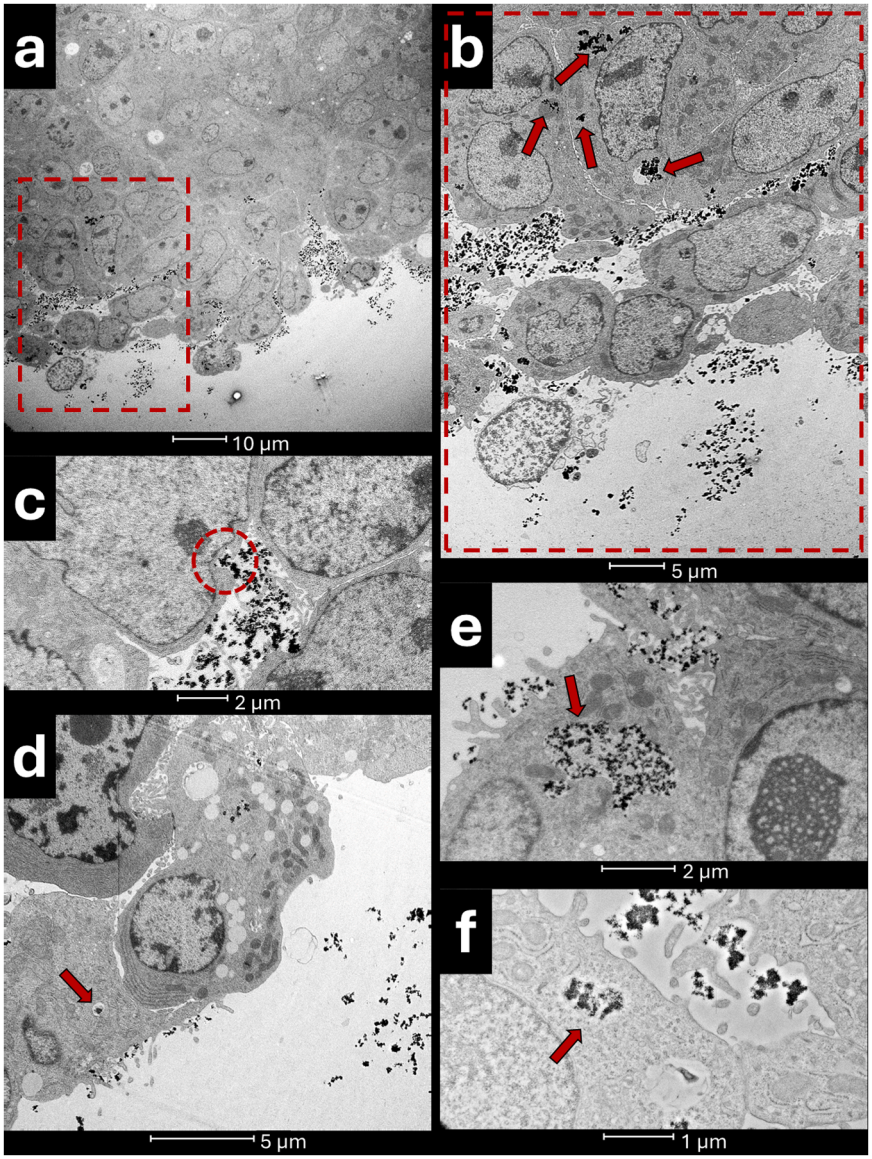

Fig. 2. Example TEM images showing MNP penetration and internalisation in HepG2 spheroids. (a) Peripheral region of a HepG2 spheroid showing ZnNPs (24 h of exposure) accumulation on the spheroid border and in the outer cell layers. (b) Close-up of the boxed area in (a), showing ZnNPs penetration into the intercellular space between adjacent cells and ZnNPs internalised by cells. (c) Example image of endosome formation, internalising ZnNPs after 24 h of exposure, marked by a red circular dashed line. (d, e, f) Representative images of intracellular endosomes containing MNPs. (d) A distinct circular endosome containing ZnNPs after 24 h of exposure, marked by a red arrow. (e) An endosome containing MnNPs (96 h of exposure). The early endosome, with visible budding-off vesicles, is marked by a red arrow. (f) An endosome containing big MnNPs aggregates after 24 h of exposure, marked by a red arrow.

corresponding to metal–oxygen stretching modes in the spinel ferrite structure.

3.2. Nanoparticle penetration into the spheroids and cellular internalisation

Transmission electron microscopy (TEM) was employed to investigate the spatial distribution of MNPs within the 3D spheroid architecture after 24 and 96 h of exposure to 50 μg/mL. Across all conditions and NP compositions (FeNPs, ZnNPs, and MnNPs), NP accumulation was predominantly confined to the peripheral cell layers of the spheroids. Internalised NP were consistently detected in the cytoplasmic compartment of the outermost cell layer, often enclosed within vesicular structures (Fig. 2). In contrast, the inner cell layers appeared devoid of NP, with no detectable electron-dense particles observed within their cytoplasm or intercellular spaces. This limited penetration was consistently observed at both exposure time points, suggesting that the compact architecture and high cell density of the spheroids constitute a significant barrier to NP diffusion beyond the surface layers. Fig. 2 depicts examples of MNPs penetration into the intercellular space between adjacent cells and cellular internalisation (Fig. 2: a,b,c,e,f), endosome formation (Fig. 2: c) and examples of MNPs-containing endosomes (Fig. 2: b,d,e,f). Additional high-resolution TEM images are available at Zenodo (10.5281/zenodo.15862860). The findings of the TEM analysis highlight a critical limitation of NP delivery in HepG2 spheroids and underscore the importance of employing advanced imaging techniques to accurately assess nanomaterial distribution within complex *in vitro* models.

3.3. Cytotoxicity of MNPs

The cytotoxicity of MNPs was evaluated in the HepG2 spheroids to determine their toxicity profile and to identify non-cytotoxic concentrations, since cytotoxic concentrations could produce misleading outcomes in genotoxicity assays. Cell viability was assessed using the CellTiter-Glo® 2.0 Assay, which measures ATP levels in culture. Since ATP is indicative of metabolic activity, the assay provides a direct estimate of the number of viable cells. Our results show that after 24 h of exposure, MnNPs exhibited the highest cytotoxicity among the tested MNPs, with an IC_{50} 43.23 ± 14.29 μg/mL, followed by ZnNPs with an IC_{50} 48.43 ± 13.86 μg/mL and FeNPs having an IC_{50} 96.37 ± 18.01 μg/mL (Fig. 3). After the 96-hour exposure, the cytotoxic effects were more pronounced, following the same pattern as at the earlier time point. MnNPs were the most cytotoxic (IC_{50} = 18.96 ± 10.49 μg/mL), followed by ZnNPs (IC_{50} = 26.20 ± 15.93 μg/mL). Again, the least cytotoxic sample was FeNPs, whose IC_{50} value was approximately 1.8 times higher (33.96 ± 14.80 μg/mL) compared to MnNPs.

Iron oxide NPs have been approved by the Food and Drug Administration (FDA) for clinical application in magnetic resonance imaging (MRI) [57], and many reports indicate that they are generally biocompatible and highly tolerated by cells [58–60]. However, other reports have highlighted their potential cytotoxic effects [61–63], a finding that

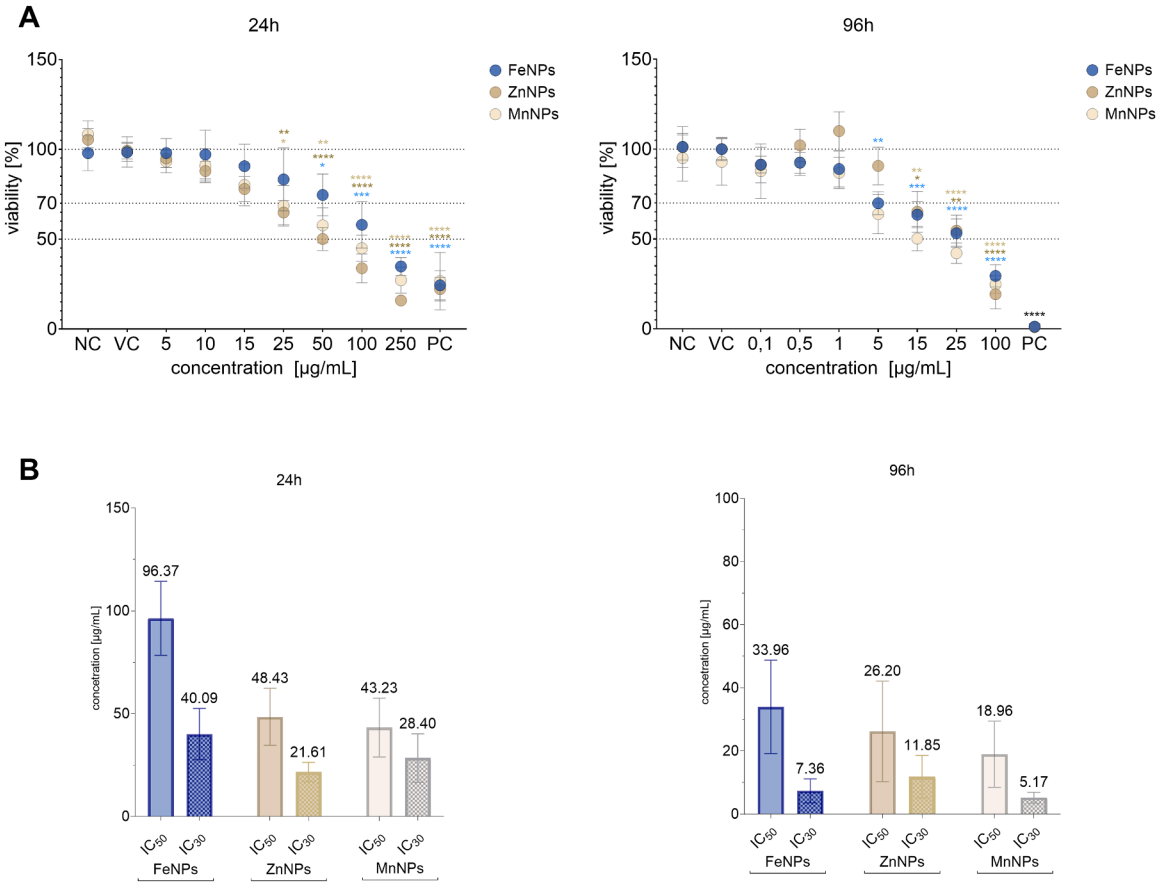

Fig. 3. Cytotoxicity of MNPs in HepG2 spheroids with corresponding IC values. A) Cell viability was determined with the CellTiter-Glo assay after exposure to graded concentrations of the MNPs (FeNPs, ZnNPs, and MnNPs) for 24 and 96 h. Data are presented relative to the vehicle control, VC (up to 3 % MilliQ water in cell media). NC – cell culture media, PC – 23 and 5 % DMSO for 24 and 96 h, respectively. * denotes statistically significant differences between the vehicle control and MNPs exposed spheroids; statistical analysis: ANOVA; Dunnett's Multiple Comparison test, *P < 0.05, **P < 0.01, ***P < 0.001, and ****P < 0.0001. B) IC_{50} and IC_{30} values were estimated using a nonparametric local regression method (LOWESS). The experiment was performed in five replicates per experimental point and repeated three times independently.

is consistent with our results. The results show that γFe_2O_3 NPs (sample FeNPs) were cytotoxic for HepG2 spheroids at concentrations above 50 μg/mL and above 5 μg/mL after 24 and 96 h of exposure, respectively.

Still, higher cytotoxicity was observed in the samples ZnNPs and MnNPs at both exposure times, which may be due to ion release. According to the literature, zinc ferrite NP decrease cell viability in a dose-dependent manner in MCF-7 cells at tested concentrations up to 200 μg/mL [15]. The decrease in cell viability in HepG2, A549, and A431 cell lines by zinc ferrite (dosage range of 10–40 μg/mL) was also shown by Alhadlaq et. al. [64]. Furthermore, Martínez-Rodríguez et al. (2019) [65] conducted an *in vitro* study on human blood cells, testing magnetite and zinc, nickel, and nickel-zinc ferrite NP at different concentrations (50, 100, and 200 μg/mL). They concluded that some of the ferrite NP at a concentration of 200 μg/mL induce hemolysis. In addition, manganese ferrite is believed to be non-toxic to cells [66]; however, inorganic manganese materials carry a risk of triggering various types of toxicity [67]. Zhang et. al. [68] reported that manganese ferrite NP decrease cell viability in RAW264.7 cells in a dose-dependent manner after 24 h of treatment at concentrations ranging from 22 to 1800 μM. Shin et. al. [66] also reported a slight decrease in cell viability when testing manganese NP in murine hepatoma Hepa1–6 cells at a 0–50 μg/mL for 24, 48, and 72 h. In contrast, *in vitro* studies conducted by Andrade et. al. [69] confirmed cytocompatibility of manganese NP in the human HEK 293 T cell line over a 0–250 μg/mL range after 24 h.

Our study shows that ZnNPs and MnNPs were cytotoxic to HepG2 spheroids at concentrations above 25 μg/mL after 24-hour exposure and above 5 μg/mL after 96 h, exhibiting higher cytotoxic potential compared to FeNPs. We assume that the observed toxic effects of all three MNPs samples are not primarily dependent on MNPs' cellular uptake, as TEM analysis showed limited internalisation. Instead, the effects are likely attributable to one or more of the following mechanisms: (i) interactions with the cell membranes, inducing mechanical stress, altering receptor signalling or membrane fluidity [70–72], (ii) ROS generation (see section below), or (iii) metal ion release from the MNPs. MNPs are known to dissolve in aqueous media, releasing potentially toxic metal ions into the surrounding media [73] and causing toxicity. On the other hand, some studies show that the particles themselves, rather than the dissolved ions, are the major source of toxicity [74]. However, further testing on ion release is needed to clarify the underlying mechanism of cytotoxicity.

3.4. Oxidative stress and oxidative damage

Given that the primary mechanism of action in metallic and metal oxide NPs is considered the generation of ROS and subsequent oxidative stress [75], one of our goals was to determine whether the tested MNPs induced ROS production and oxidative damage.

Reactive oxygen species (ROS) levels in HepG2 spheroids, measured using the DCFH-DA probe, are presented in Fig. 4, along with MDA measurements (Fig. 5), a marker of lipid peroxidation. DCFH-DA is a fluorescent probe that indicates oxidation by hydrogen peroxide, peroxynitrite, or hydroxyl radicals. Superoxide anions can also contribute to DCFH-DA oxidation, albeit to a lesser degree [76]. Our results showed no significant increase in ROS levels after 2 h of exposure in any of the tested samples, while after 4 h, a dose-dependent increase was observed in FeNPs and MnNPs-treated samples. What is also intriguing is that a slight but non-significant increase in ROS was observed already after 2 h of exposure to FeNPs, implicating that FeNPs are the most potent and rapid inducers of ROS among the tested samples. Their higher rate of ROS production compared to ZnNPs and MnNPs could be explained by the electronic structure of NP and their redox activity. Specifically, the surfaces of iron oxide NP can catalytically generate ROS through the Fenton and Haber–Weiss reactions ($Fe^{2+} \rightleftharpoons Fe^{3+}$ redox cycling), thus having high redox activity [77]. Furthermore, Mn ions are known to accelerate the Fenton reaction [78], which may explain the significant dose-dependent increase in ROS after 4 h of exposure to MnNPs. The difference in the rate of ROS generation between FeNPs and MnNPs is probably due to the kinetic release of ions from NP. We assume that FeNPs dissolve and release Fe ions more readily, leading to faster Fenton-like reactions, while Fe and Mn ions from MnNPs are released more slowly, delaying the onset of ROS production [79]. On the other hand, ZnNPs include Zn ions, which can directly scavenge ROS, reducing their levels and preventing oxidative damage to cellular components [80]. Thus, incorporating Zn ions can modulate iron redox activity, potentially altering ROS levels. Our results also support this, as there was no significant elevation of ROS after 2 and 4 h of exposure to ZnNPs.

These findings are in line with previous electron paramagnetic resonance (EPR) analyses on the same Mn- and Zn-ferrite NP, which showed distinct ROS profiles: MnNPs generated significant amounts of hydroperoxyl radicals (•OOH), while ZnNPs exhibited negligible radical formation [53]. This difference is likely due to the redox-active nature of Mn^{2+} versus the redox-inert behaviour of Zn^{2+}, whose stable d^{1} °

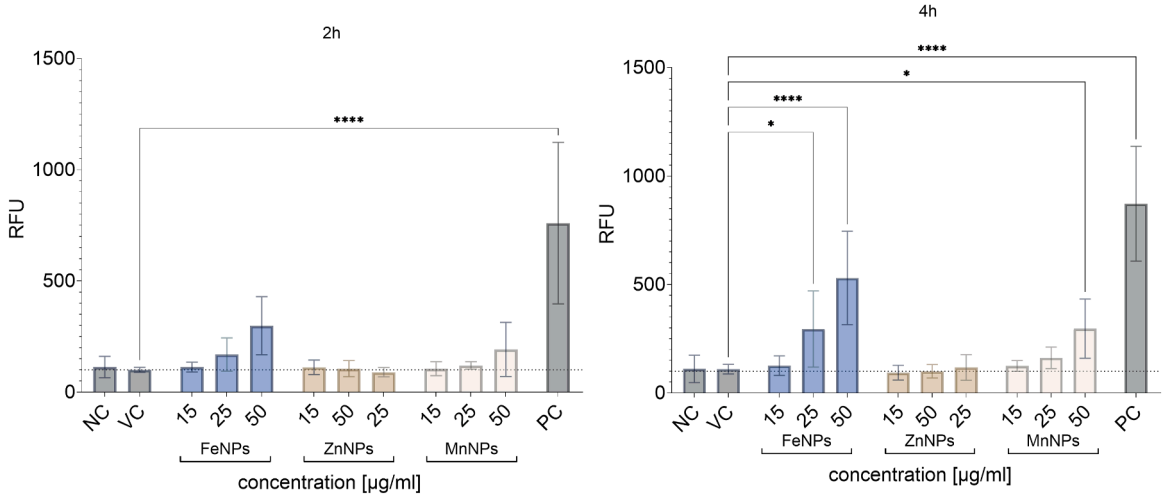

Fig. 4. Generation of reactive oxygen species (ROS). The DCFH-DA assay was used to measure elevation in ROS production after 2- and 4-hour exposure to graded concentrations of FeNPs, ZnNPs, and MnNPs samples. The measurements are expressed as relative fluorescence units (RFU). tBHP (1 mM) was used as the positive control (PC); NC – negative control (cell medium). Statistically significant difference (Kruskal-Wallis and Dunn's post-test) between MNPs-exposed cells and vehicle control, VC (up to 3 % MilliQ water in cell media), is indicated by *$P < 0.05$ and ****$P < 0.0001$. The experiment was performed in five replicates per experimental point and repeated three times independently.

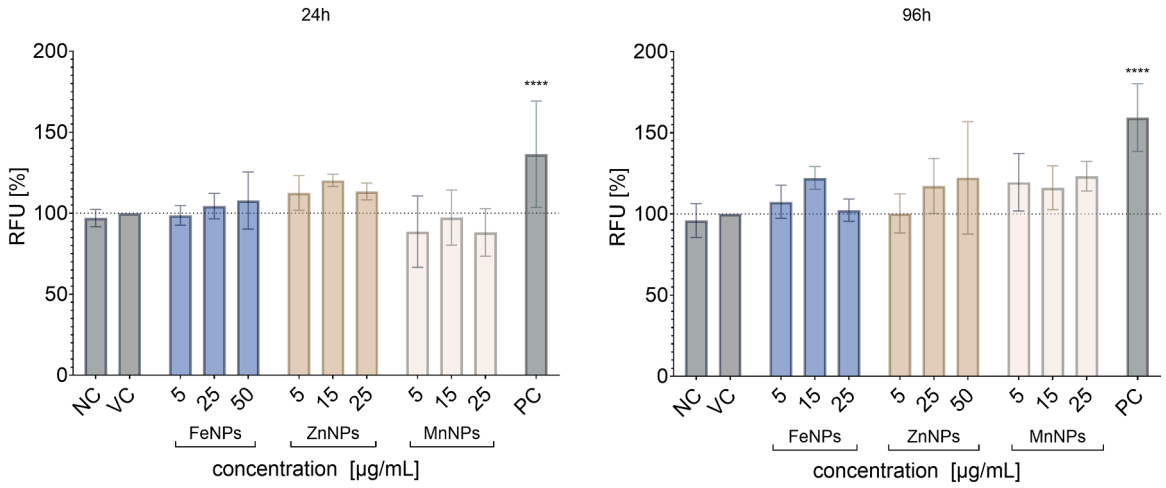

Fig. 5. Lipid peroxidation. MDA, a marker of lipid peroxidation, was used to evaluate oxidation of lipids after 24- and 96-hour exposure to graded concentrations of FeNPs, ZnNPs, and MnNPs samples. The measurements are expressed as relative fluorescence units (RFU) in percentage of the vehicle control (VC, up to 3 % MilliQ water in cell media). tBHP (1 mM) was used as the positive control (PC); NC – negative control (cell medium). Statistically significant difference (Kruskal-Wallis and Dunn's post-test) between MNPs-exposed cells and VC is indicated by ****$P < 0.0001$. The experiment was performed in three replicates per experimental point and repeated three times independently.

electronic configuration prevents its participation in electron transfer processes [81,82]. Such surface passivation by Zn may account for the absence of oxidative stress markers in ZnNPs, despite their cytotoxicity, suggesting alternative, non-oxidative cellular stress mechanisms.

Furthermore, previous studies have suggested that various NP (including ferrites) can induce ROS, leading to cell damage through indirect mechanisms [83]. Since our results indicated ROS production by two of the three tested MNPs, we measured MDA as a marker of lipid peroxidation and hence excessive oxidative stress. As can be seen from Fig. 5, there was no significant increase in MDA formation at any of the tested concentrations or for any MNPs type, neither at 24 nor 96 h of exposure.

Cells maintain a robust antioxidant defence system within the cytoplasm and cellular organelles, comprising enzymatic and non-enzymatic antioxidants that synergise with ROS and preserve redox balance [84]. Key antioxidant enzymes include superoxide dismutase (SOD), catalase (CAT), and various peroxidases, such as glutathione peroxidase (GPX1) [85]. Among non-enzymatic antioxidants, glutathione (GSH) plays a central role. Its biosynthesis is tightly regulated by glutamate cysteine ligase (GCLC), while its redox cycling depends on glutathione reductase (GSR) [86]. GSR is essential for converting oxidised glutathione (GSSG) back to its reduced form, GSH, thereby maintaining the intracellular redox balance and protecting cells from oxidative damage [87]. Expression profiling of oxidative stress-response genes (*CAT, SOD1, GCLC, GSR,* and *GPX1*) (Fig. 8) revealed no significant upregulation across all samples, concentrations, and timepoints, except for *GPX1*, which was upregulated after 24 h of exposure to the highest FeNPs concentration (50 µg/mL). *GPX1* is extremely sensitive, and its increased expression can be triggered by a subtle, non-damaging redox signal or metal ion-mediated stress [88]. This is consistent with the induction of ROS observed after exposure to FeNPs, indicating activation of antioxidant defence mechanisms. If these antioxidant defences are active and effective, ROS levels may rise transiently, without causing lipid damage, which could explain our results on ROS and MDA measurements. Furthermore, cells possess enzymatic systems that repair or remove oxidised lipids before they accumulate. By reducing lipid hydroperoxides, these enzymes prevent further oxidation and free radical formation. This reduction is carried out by diverse antioxidant enzymes, including selenocysteine-containing proteins like glutathione peroxidase (GPX) [89]. Finally, although the DCFH-DA assay detected a significant rise in ROS, and transcriptomic analysis indicated the activation of antioxidant defence mechanisms, ROS production was likely below a critical threshold required to induce lipid peroxidation.

3.5. Potential in vitro genotoxicity of FeNPs, ZnNPs, and MnNPs

Given the increasing biomedical and technological applications of MNPs, ensuring their safety is a critical prerequisite for their translation to clinical and industrial use. Among the different aspects of nanosafety, genotoxicity assessment is a key priority, as DNA damage can lead to long-term health effects, including carcinogenesis. Our study examined the genotoxicity potential of the tested MNPs using the comet assay and γH2Ax and p-H3 assays, coupled with transcriptomics analysis of genes deregulated in response to DNA damage and/or oxidative stress. Concentrations of MNPs for genotoxicity testing were determined based on cytotoxicity measurements, specifically those that did not decrease cell viability by more than 25–30 %. The comet assay, also known as single-cell gel electrophoresis, is a simple, rapid and sensitive technique for the detection of DNA single- and double-strand breaks (SSBs/DSBs), alkali-labile sites, and cross-linking sites in a single individual cell [90]. The assay can also detect transient SSBs, emerging during DNA damage repair processes [91]. Our results (Fig. 6) show a slight but statistically significant increase in DNA damage for ZnNPs and MnNPs at the highest concentration tested after 24 h of exposure, while FeNPs did not induce detectable DNA damage. On the other hand, all tested MNPs induced a significant increase in DNA damage after 96 h of exposure. Previous studies have shown that metal-based NP, like Ag-NP, CuO-NP, and ZnO-NP, tend to release their metallic ions while they dissolve in the cytoplasm and that the interaction of these ions with DNA is the primary cause of genotoxicity [92]. Furthermore, Gosh and coworkers (2019) confirmed the induction of DNA strand breaks by Mn oxide NP due to Mn dissolution, uptake and internalisation in *Physcomitrella patens,* a model plant system used for evolutionary developmental genetics [93]. A similar study with Mn oxide NP was conducted by Alarifi (2017), who showed that Mn oxide NP induce DNA damage in SH-SY5Y cells [94]. Our results align with earlier studies indicating that MNPs can induce DNA damage, likely through mechanisms involving metal ion release and ROS production. Although produced at low levels, the sustained elevation of ROS, as indicated by our results, may have led to oxidative DNA damage and transient lesions, resulting from their elevated repair, contributing to the DNA damage observed in the comet assay. However, caution is warranted when interpreting the significant DNA damage observed after 96 h of exposure. Extended exposure may compromise the cytoskeleton and nuclear envelope, reducing nuclear stability and

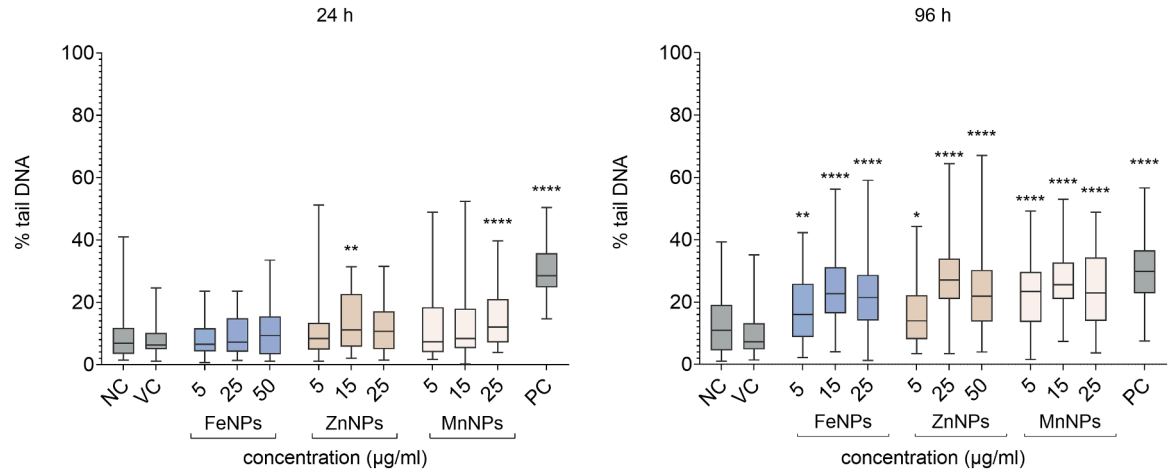

Fig. 6. DNA damage induction by FeNPs, ZnNPs, and MnNPs samples in HepG2 spheroids. DNA damage was assessed by the comet assay after exposure to graded concentrations of the MNPs (FeNPs, ZnNPs, and MnNPs) for 24 and 96 h. Data are expressed as % of DNA in the "comet tail" and presented as quantile box plots (95 % confidence interval). Benzo[*a*]pyrene (30 and 5 μM for 24 and 96 h, respectively) was used as the positive control (PC), and NC represents cell medium. Fifty cells were analysed per experimental point in the three independent experiments. A statistically significant difference (Kruskal-Wallis and Dunn's post-test) between MNPs-exposed cells and the vehicle control, VC (up to 3 % MilliQ water in cell media), is indicated by *P < 0.05, **P < 0.01, ***P < 0.001, and ****P < 0.0001.

altering chromatin organization [95].

To confirm whether the tested MNPs induce DNA DSBs or aneugenic effects, we assessed γH2AX, a DSB biomarker reflecting clastogenic effects, and p-H3, a marker of mitotic cells indicative of chromosome missegregation, using immunofluorescence labelling and flow cytometric analysis. Among various types of DNA damage, DSBs are considered the most harmful, as they are inherently challenging to repair. Their occurrence can lead to genomic instability and mutations, increasing the risk of tumorigenesis [91]. Efficient repair of DNA DSBs requires a coordinated DNA damage response, which includes phosphorylation of a component of the histone octamer in nucleosomes, histone H2Ax, forming γH2Ax [96]. The phosphorylated form γH2AX accumulates at DSB sites and forms foci that directly correlate with the amount of DSBs [97]. Therefore, γH2AX is a well-established biomarker of DSB induction and clastogenic activity. During mitosis, histone H3 undergoes phosphorylation to facilitate chromosome condensation and segregation [98]. As a biomarker of mitotic cells, phosphorylated H3 (p-H3) is widely used as a surrogate marker for aneugenic compounds [99]. Namely, aneugenic compounds induced either an increase or a decrease in p-H3, depending on their mode of action, because they can interfere with the mitotic machinery, disrupting spindle formation, centromere attachment, or chromosome segregation [100].

Analysis of γH2AX (Fig. 7A) and p-H3-positive events (Fig. 7B) after 24 and 96 h of exposure to the tested MNPs showed that none of them induced DSBs or increased the percentage of p-H3-positive events at any of the concentrations tested. Based on these results, the slight increase in DNA damage observed in the comet assay could be due to oxidative DNA damage caused by ROS generated from the tested MNPs. While clastogenic and aneugenic activities can be excluded, the exact mechanism underlying the DNA damage detected by the comet assay remains unclear.

In addition to assessing the previously mentioned endpoints, toxicogenomic analyses were conducted to identify gene expression changes linked to a (geno)toxicological response. Recent research indicates that gene expression profiling is a powerful approach for assessing human health risks, offering both qualitative and quantitative information about the specific biological pathways and molecular mechanisms triggered by the tested material [101]. This approach allows the identification of early molecular events that may precede overt toxicity, supporting a mechanistic understanding of adverse outcomes and facilitating the development of predictive biomarkers for hazard assessment. In the present study, the expression of selected DNA damage-responsive genes (*TP53, MDM2, GADD45a, CDKN1A, OGG1, and JUNB*), apoptosis-related genes (*BCL2* and *BAX*) and oxidative stress response genes (*SOD1, CAT, GPX1, GCLC,* and *GSR* – discussed above) was evaluated upon exposure to MNPs. These genes encode proteins that play vital roles in maintaining cellular homeostasis and responding to genotoxic stress. The wild-type *TP53* gene encodes p53 protein, a transcription factor crucial in coordinating diverse cellular responses, including DNA repair, cell cycle arrest, senescence, cell death, differentiation, and metabolism. By suppressing tumorigenesis and preserving genomic integrity, p53 is also known as the "guardian of the genome" [102,103]. MDM2 (mouse double minute 2 homolog) is a negative regulator of the tumour suppressor p53 [104], modulating its activity to maintain cellular homeostasis. *GADD45a* belongs to a family of genes whose transcript levels are increased in response to growth arrest and DNA-damaging stress [105]. Additionally, it plays a crucial role in the stabilisation of the p53 protein [29], thereby reinforcing the cellular DNA damage response. *CDKN1A* is a potent cyclin-dependent kinase inhibitor that regulates cell cycle progression at the G1 phase [28]. Furthermore, *OGG1* encodes for 8-oxoguanine glycosylase, a bifunctional glycosylase vital for the recognition and excision of oxidised DNA bases, thereby maintaining genomic integrity [106]. Finally, *JUNB,* a member of the AP-1 (activator protein-1) family of dimeric transcription factors, is best known as a cell proliferation inhibitor, senescence inducer, and a tumour suppressor [107].

Expression levels of tested genes were visualised using heatmaps (Fig. 8), and the corresponding induction factors with p-values are summarised in Table S3 and Table S4. At 24 h, no significant changes in gene expression were observed for DNA damage-responsive and apoptosis-related genes, except for *GADD45A*, which showed slight upregulation across all tested samples. The most pronounced increase (fold change ≈1.5) was detected in FeNPs at 50 μg/mL, suggesting activation of a p53-mediated DNA damage response. Notably, TP53 mRNA levels remained unchanged at both 24 and 96 h, consistent with the well-established concept that p53 is primarily regulated post-translationally [108,109]. Additionally, *BCL2* was modestly upregulated in cells exposed to FeNPs and ZnNPs, with fold changes above 1.5, particularly in FeNPs at 50 μg/mL, potentially reflecting a pro-survival adaptation to NP-induced stress.

By 96 h, a broader pattern of gene activation emerged. *GADD45A* and *CDKN1A* were consistently but modestly upregulated across all samples, with the strongest induction observed in ZnNPs at 50 μg/mL. Importantly, *BCL2* expression increased significantly in cells exposed to

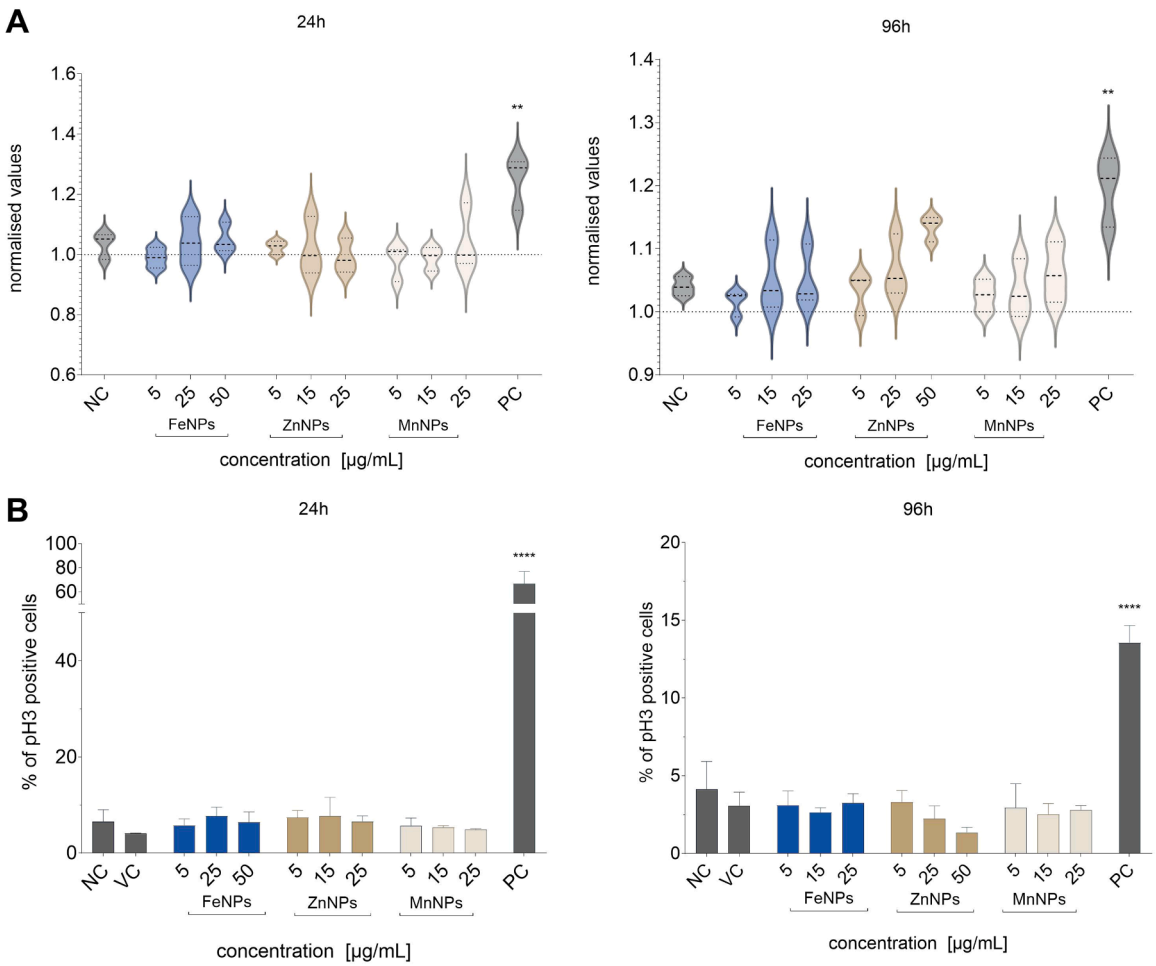

Fig. 7. Potential induction of DNA double-strand breaks (DSBs) and p-H3 positive events by MNPs in HepG2 spheroids. A) Flow cytometric analysis of γH2AX expression in individual cells after exposure to graded concentrations (5–50 µg/mL) of FeNPs, ZnNPs, and MnNPs for 24 and 96 h is shown. Etoposide (1.7 µM) was used as a positive control (PC). Data are displayed as violin plots representing normalised fluorescence intensity relative to the vehicle control (dashed line; up to 3 % Milli-Q water in cell medium). The width of a "violin" reflects value frequency; the central line marks the median, while the upper and lower lines indicate the 75th and 25th quartiles. Significant differences versus control were assessed by ANOVA with Dunnett's post-test (**P < 0.01, ***P < 0.001). B) The mean percentage of p-H3-positive cells following exposure to increasing concentrations (5–50 µg/mL) of FeNPs, ZnNPs, and MnNPs for 24 and 96 h, as measured by flow cytometry, is shown. Colchicine (0.1 mM) served as a positive control (PC). Statistically significant differences compared to the vehicle control (up to 3 % Milli-Q water in cell medium) were determined by ANOVA, followed by Dunnett's post-test and are denoted as ****P < 0.0001. Each experiment was carried out independently three times, and 10,000 events were acquired per sample.

ZnNPs at 25 and 50 µg/mL, and to a lesser extent in MnNPs at 15 and 25 µg/mL, with fold changes exceeding 1.5 and reaching statistical significance (*p < 0.001). This pattern suggests an anti-apoptotic response or adaptive mechanism to counteract prolonged NP exposure. *BCL2* encodes a key anti-apoptotic protein, while *BAX*, a pro-apoptotic counterpart, promotes apoptosis by antagonising *BCL2* function [110]. The observed expression patterns reflect a cellular effort to prevent apoptosis, likely facilitating DNA repair and maintaining survival under sustained stress. This is supported by the slight elevation of DNA damage response genes at 96 h. Overall, these data indicate that MNPs exposure triggers dynamic, time- and dose-dependent transcriptional responses, reflecting the activation of DNA damage repair pathways and anti-apoptotic mechanisms aimed at preserving cellular viability under prolonged stress.

In conclusion, assessing (geno)toxic potential of MNPs remains a critical aspect in evaluating their safety for biomedical and other applications. Our findings indicate that the tested MNPs exhibit no significant genotoxic effects in a 3D human hepatic model. In line with previous studies suggesting their use in biomedical applications, such as targeted drug delivery, imaging systems or magnetic hyperthermia [22], these results support the potential feasibility of these applications. Nevertheless, we emphasise that this represents only a small piece of the overall safety evaluation, and further investigations using diverse advanced *in vitro* models are necessary. Such studies will provide a more comprehensive and physiologically relevant understanding of MNPs' interactions in the human body, considering the complex interplay between their physicochemical properties, composition, cellular uptake, exposure conditions, and the resulting cellular responses.

To advance the field, more systematic and standardised approaches are needed to fully characterize the spectrum of potential toxic effects. Integrating advanced imaging techniques, omics technologies, and *in vitro/in vivo* correlation models would deepen our understanding of the mechanistic pathways underlying MNP-induced toxicity. Furthermore, evaluating long-term exposures and the role of NP-induced epigenetic changes would provide valuable insights into their biological impact. Finally, incorporating predictive toxicology frameworks and safe-by-design strategies would support the development of MNPs with optimized efficacy and minimized adverse effects, bridging the gap between fundamental research and safe translational applications.

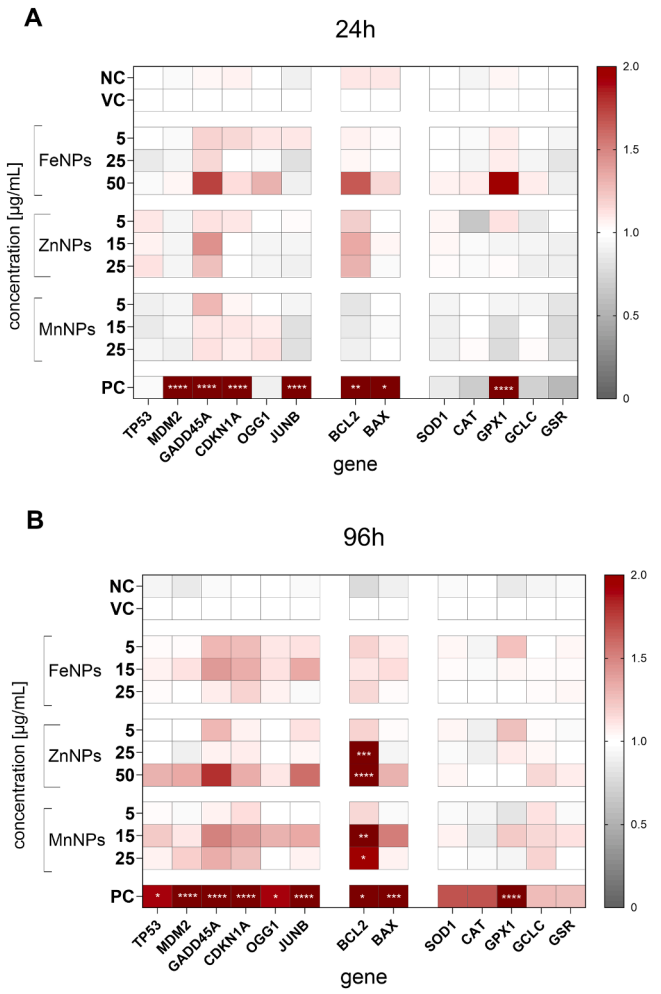

Fig. 8. Heatmaps illustrate the expression profiles of DNA damage response, apoptosis-related, and oxidative stress response genes following (A) 24 h and (B) 96 h of exposure. Gene expression changes are shown as fold change relative to the vehicle control (VC; ≤3 % MilliQ water), which is normalised to 1 and represented in white. Upregulation is visualised in shades of red to dark red, while downregulation appears in grey tones, according to the accompanying scale. NC denotes the negative control (growth medium), and PC represents the positive control (10 µg/mL etoposide). Statistically significant differences compared to the vehicle control (≤3 % Milli-Q water in cell medium) were determined by two-way ANOVA and Fisher's LSD test, denoted as *P < 0.05, **P < 0.01, ***P < 0.001. The experiment was repeated three times independently.

List of abbreviations

FTIR, Fourier-transform infrared; ICP-OES, Inductively Coupled Plasma–Optical Emission Spectroscopy; MDA, malondialdehyde; MNPs, metal ferrite nanoparticles; tBHP, tert-Butyl hydroperoxide; XRD, X-ray diffraction

Study limitations

This study has certain limitations. As the experiments were conducted *in vitro* using a 3D HepG2 cell model, direct translation to whole-organism physiology should be approached with caution. The study focused on relatively short-term exposures, while long-term effects are yet to be studied. Finally, nanoparticle behaviour in culture conditions (such as potential agglomeration or protein corona formation over time) was not fully examined and will require further characterisation in future work.

CRediT authorship contribution statement

Domen Hočevar: Software, Methodology, Data curation. **Katja Kološa:** Writing – review & editing, Supervision, Data curation. **Stern Alja:** Writing – review & editing, Supervision, Software, Methodology, Investigation, Conceptualization, Formal analysis. **Bojana Žegura:** Writing – review & editing, Supervision, Resources, Funding acquisition, Conceptualization. **Iza Rozman:** Writing – original draft, Visualization, Validation, Software, Methodology, Investigation, Formal analysis, Data curation. **Morales Maria del Puerto:** Writing – review & editing, Supervision, Resources, Investigation, Conceptualization. **Alvaro Gallo-Cordova:** Writing – review & editing, Visualization, Validation, Software, Methodology, Investigation, Formal analysis, Data curation. **Gerardo F. Goya:** Writing – review & editing, Visualization, Supervision, Resources, Investigation, Funding acquisition, Conceptualization. **Marco A. Morales Ovalle:** Visualization, Software, Methodology, Investigation, Data curation.

Consent for publication

Not applicable.

Ethics approval and consent to participate

No human participants and/or animals were involved in the study. The HepG2 cell line, obtained from the ATCC-Cell bank, was used in the study.

Funding

This study was supported by the European Union H2020-MSCA NESTOR project (101007629), the HE CutCancer project (101079113), and the Slovenian Research and Innovation Agency Research Core Funding No. P1–0245, and projects ARIS J1–4395 and ARIS MR grant to IR.

Declaration of Competing Interest

The authknown competing financial interests or personal relationships that could ors declare that they have no have appeared to influence the work reported in this paper.

Acknowledgements

Not applicable.

Appendix A. Supporting information

Supplementary data associated with this article can be found in the online version at doi:10.1016/j.biopha.2025.118950.

Data availability

Raw data are available from the corresponding author and Zenodo (TEM images - 10.5281/zenodo.15862860, comet assay data - 10.5281/zenodo.17896231, and toxicogenomic data - 10.5281/zenodo.17815525).

References

[1] K. Asghar, M. Qasim, D. Das, Preparation and characterization of mesoporous magnetic MnFe2O4@mSiO2 nanocomposite for drug delivery application, Mater. Today Proc. 26 (2020) 87–93, https://doi.org/10.1016/j.matpr.2019.05.380.
[2] A.B. Naik, P.P. Naik, S.S. Hasolkar, D. Naik, Structural, magnetic and electrical properties along with antifungal activity & adsorption ability of cobalt doped manganese ferrite nanoparticles synthesized using combustion route, Ceram. Int 46 (2020) 21046–21055, https://doi.org/10.1016/j.ceramint.2020.05.177.

[3] T. Dippong, E.A. Levei, O. Cadar, Recent advances in synthesis and applications of MFe2O4 (M = Co, Cu, Mn, Ni, Zn) nanoparticles, Nanomaterials 11 (2021) 1560, https://doi.org/10.3390/nano11061560.
[4] D. S. G, B M. A comprehensive review on current trends in greener and sustainable synthesis of ferrite nanoparticles and their promising applications, Results Eng. 21 (2024) 101702, https://doi.org/10.1016/j.rineng.2023.101702.
[5] V. Jeseentharani, M. George, B. Jeyaraj, A. Dayalan, K.S. Nagaraja, Synthesis of metal ferrite (MFe 2 O 4, M = Co, Cu, Mg, Ni, Zn) nanoparticles as humidity sensor materials, J. Exp. Nanosci. 8 (2013) 358–370, https://doi.org/10.1080/17458080.2012.690893.
[6] T. Dippong, Characterization and applications of metal ferrite nanocomposites, Nanomaterials 12 (2021), https://doi.org/10.3390/nano12010107.
[7] P. Chand, S. Vaish, P. Kumar, Structural, optical and dielectric properties of transition metal (MFe2O4; M = Co, Ni and Zn) nanoferrites, Phys. B Condens Matter 524 (2017) 53–63, https://doi.org/10.1016/j.physb.2017.08.060.
[8] P.-Y. Li, L. Li, Y.-Z. Wang, Traditional uses, chemical compositions and pharmacological activities of Dendrobium: a review, J. Ethnopharmacol. 310 (2023) 116382, https://doi.org/10.1016/j.jep.2023.116382.
[9] P.C. Srivastava, R. Dwivedi, A. Srivastava, S. Kumar, M. Shrivastva, Relationships of labile pool of Mn with some general soil properties and extractable soil Mn contents, J. Radio. Nucl. Chem. 290 (2011) 149–151, https://doi.org/10.1007/s10967-011-1168-x.
[10] O. Kakhlon, Z.I. Cabantchik, The labile iron pool: characterization, measurement, and participation in cellular processes1 1This article is part of a series of reviews on "Iron and Cellular Redox Status." The full list of papers may be found on the homepage of the journal, Free Radic. Biol. Med 33 (2002) 1037–1046, https://doi.org/10.1016/S0891-5849(02)01006-7.
[11] B. Turan, E. Tuncay, Impact of labile zinc on heart function: from physiology to pathophysiology, Int. J. Mol. Sci. 18 (2017) 2395, https://doi.org/10.3390/ijms18112395.
[12] A.R. Liandi, A.H. Cahyana, A.J.F. Kusumah, A. Lupitasari, D.N. Alfariza, R. Nuraini, R.W. Sari, F.C. Kusumasari, Recent trends of spinel ferrites (MFe2O4: Mn, Co, Ni, Cu, Zn) applications as an environmentally friendly catalyst in multicomponent reactions: a review, Case Stud. Chem. Environ. Eng. 7 (2023) 100303, https://doi.org/10.1016/j.cscee.2023.100303.
[13] S.N. Pund, P.A. Nagwade, A.V. Nagawade, S.R. Thopate, A.V. Bagade, Preparation techniques for zinc ferrites and their applications: a review, Mater. Today Proc. 60 (2022) 2194–2208, https://doi.org/10.1016/j.matpr.2022.02.444.
[14] X. Liu, J. Liu, S. Zhang, Z. Nan, Q. Shi, Structural, magnetic, and thermodynamic evolutions of Zn-doped Fe3O4 nanoparticles synthesized using a one-step solvothermal method, J. Phys. Chem. C. 120 (2016) 1328–1341, https://doi.org/10.1021/acs.jpcc.5b10618.
[15] J. Ahmad, R. Wahab, M. A. Siddiqui, M. Ahamed, Cytotoxicity and apoptosis induction of zinc ferrite nanoparticle through the oxidative stress pathway in human breast cancer cells, J. King Saud. Univ. Sci. 36 (2024) 103047, https://doi.org/10.1016/j.jksus.2023.103047.
[16] H.A. Alhadlaq, M.J. Akhtar, M. Ahamed, Zinc ferrite nanoparticle-induced cytotoxicity and oxidative stress in different human cells, Cell Biosci. 5 (2015) 55, https://doi.org/10.1186/s13578-015-0046-6.
[17] S. Kanagesan, S. Aziz, M. Hashim, I. Ismail, S. Tamilselvan, N. Alitheen, M. Swamy, B. Purna Chandra Rao, Synthesis, characterization and in vitro evaluation of manganese ferrite (MnFe2O4) nanoparticles for their biocompatibility with murine breast cancer cells (4T1), Molecules 21 (2016) 312, https://doi.org/10.3390/molecules21030312.
[18] A. Manohar, V. Vijayakanth, P. Manivasagan, E.-S. Jang, B. Hari, M. Gu, K. H. Kim, Investigation on the physico-chemical properties, hyperthermia and cytotoxicity study of magnesium doped manganese ferrite nanoparticles, Mater. Chem. Phys. 287 (2022) 126295, https://doi.org/10.1016/j.matchemphys.2022.126295.
[19] M. Abudayyak, T. Altınçekiç Gürkaynak, G. Özhan, Assessment of cellular responses in kidney cells exposed to cobalt oxide nanoparticles, 537, Marmara Pharm. J. 21 (2017) 537, https://doi.org/10.12991/marupj.318619.
[20] B. Sanz-Sagué, A. Sáenz- Hernández, A.C. Moreno Maldonado, J.A. Fuentes-García, J.M. Nuñez, B. Zegura, A. Stern, K. Kolosa, I. Rozman, T.E. Torres, G. F. Goya, Genotoxicity and heating Performance of VxFe3-xO4 nanoparticles in Health applications, Chem. Biol. Inter. 394 (2024) 110977, https://doi.org/10.1016/j.cbi.2024.110977.
[21] F. Gamberoni, M. Borgese, C. Pagiatakis, I. Armenia, V. Grazù, R. Gornati, S. Serio, R. Papait, G. Bernardini, Iron oxide nanoparticles with and without cobalt functionalization provoke changes in the transcription profile via epigenetic modulation of enhancer activity, Nano Lett. 23 (2023) 9151–9159, https://doi.org/10.1021/acs.nanolett.3c01967.
[22] S.R. Mokhosi, W. Mdlalose, A. Nhlapo, M. Singh, Advances in the synthesis and application of magnetic ferrite nanoparticles for cancer therapy, Pharmaceutics 14 (2022) 937, https://doi.org/10.3390/pharmaceutics14050937.
[23] Á. Gallo-Cordova, A. Espinosa, A. Serrano, L. Gutiérrez, N. Menéndez, M. del Puerto Morales, E. Mazarío, New insights into the structural analysis of maghemite and (MFe 2 O 4, M = Co, Zn) ferrite nanoparticles synthesized by a microwave-assisted polyol process, Mater. Chem. Front 4 (2020) 3063–3073, https://doi.org/10.1039/D0QM00460J.
[24] R. Costo, M.P. Morales, S. Veintemillas-Verdaguer, Improving magnetic properties of ultrasmall magnetic nanoparticles by biocompatible coatings, J. Appl. Phys. 117 (2015), https://doi.org/10.1063/1.4908132.
[25] M. Štampar, J. Tomc, M. Filipič, B. Žegura, Development of in vitro 3D cell model from hepatocellular carcinoma (HepG2) cell line and its application for genotoxicity testing, Arch. Toxicol. 93 (2019) 3321–3333, https://doi.org/10.1007/s00204-019-02576-6.
[26] M.J. Burgum, C. Ulrich, N. Partosa, S.J. Evans, C. Gomes, S.B. Seiffert, R. Landsiedel, N. Honarvar, S.H. Doak, Adapting the *in vitro* micronucleus assay (OECD Test Guideline No. 487) for testing of manufactured nanomaterials: recommendations for best practices, Mutagenesis 39 (2024) 205–217, https://doi.org/10.1093/mutage/geae010.
[27] M. Štampar, J. Tomc, M. Filipič, B. Žegura, Development of in vitro 3D cell model from hepatocellular carcinoma (HepG2) cell line and its application for genotoxicity testing, Arch. Toxicol. 93 (2019) 3321–3333, https://doi.org/10.1007/s00204-019-02576-6.
[28] National Center for Biotechnology Information. CDK1 cyclin dependent kinase 1 [Homo sapiens (human)] [Online]. [date unknown]. ⟨https://www.ncbi.nlm.nih.gov/gene/1026⟩ [7 Apr. 2025].
[29] S. Jin, L. Mazzacurati, X. Zhu, T. Tong, Y. Song, S. Shujuan, K.L. Petrik, B. Rajasekaran, M. Wu, Q. Zhan, Gadd45a contributes to p53 stabilization in response to DNA damage, Oncogene 22 (2003) 8536–8540, https://doi.org/10.1038/sj.onc.1206907.
[30] A. Štern, M. Novak, K. Kološa, J. Trontelj, S. Žabkar, T. Šentjurc, M. Filipič, B. Žegura, Exploring the safety of cannabidiol (CBD): a comprehensive in vitro evaluation of the genotoxic and mutagenic potential of a CBD isolate and extract from Cannabis sativa L, Biomed. Pharmacother. 177 (2024) 116969, https://doi.org/10.1016/j.biopha.2024.116969.
[31] S. Riaz, S. Ali, M. Summer, U. Akhtar, S. Noor, R. Haqqi, M.A. Farooq, I. Sardar, Multifunctional magnetic nanoparticles for targeted drug delivery against cancer: a review of mechanisms, applications, consequences, limitations, and tailoring strategies, Ann. Biomed. Eng. 53 (2025) 1291–1327, https://doi.org/10.1007/s10439-025-03712-3.
[32] W. Graham, M. Torbett-Dougherty, A. Islam, S. Soleimani, T.A. Bruce-Tagoe, J. A. Johnson, Magnetic NAnoparticles and Drug Delivery Systems for Anti-cancer Applications: A Review, Nanomaterials 15 (2025) 285, https://doi.org/10.3390/nano15040285.
[33] J.F. Liu, B. Jang, D. Issadore, A. Tsourkas, Use of magnetic fields and nanoparticles to trigger drug release and improve tumor targeting, WIREs Nanomed. Nanobiotechnol. 11 (2019), https://doi.org/10.1002/wnan.1571.
[34] L. Dou, X. Zhang, M.M. Zangeneh, Y. Zhang, Efficient biogenesis of Cu2O nanoparticles using extract of Camellia sinensis leaf: evaluation of catalytic, cytotoxicity, antioxidant, and anti-human ovarian cancer properties, Bioorg. Chem. 106 (2021) 104468, https://doi.org/10.1016/j.bioorg.2020.104468.
[35] Y. Li, N. Li, W. Jiang, G. Ma, M.M. Zangeneh, In situ decorated Au NPs on pectin-modified Fe3O4 NPs as a novel magnetic nanocomposite (Fe3O4/Pectin/Au) for catalytic reduction of nitroarenes and investigation of its anti-human lung cancer activities, Int J. Biol. Macromol. 163 (2020) 2162–2171, https://doi.org/10.1016/j.ijbiomac.2020.09.102.
[36] J. Bai, X. Gongsun, L. Xue, M.M. Zangeneh, Introducing a modern chemotherapeutic drug formulated by iron nanoparticles for the treatment of human lung cancer, J. Exp. Nanosci. 16 (2021) 397–409, https://doi.org/10.1080/17458080.2021.1998460.
[37] A. Ahmeda, A. Zangeneh, M.M. Zangeneh, Characterization and anti-acute T cell leukemia properties of silver nanoparticles synthesized by a green approach for bioremediation applications: introducing a new chemotherapeutic drug for clinical trial studies, Appl. Organomet Chem. 34 (2020), https://doi.org/10.1002/aoc.5374.
[38] F.S. Nejad, M. Alizade-Harakiyan, M. Haghi, R. Ebrahimi, M.M. Zangeneh, A. Farajollahi, R. Fathi, R. Mohammadi, S.S. Miandoab, M.H. Asl, B. Divband, A. Ahmadi, Investigating the efficacy of silver *Anethum graveolens* nano-extract in colon cancer radiotherapy, ChemistrySelect 10 (2025), https://doi.org/10.1002/slct.202405345.
[39] A. Ahmeda, M.M. Zangeneh, A. Zangeneh, Green formulation and chemical characterization of <scp> Lens culinaris </scp> seed aqueous extract conjugated gold nanoparticles for the treatment of acute myeloid leukemia in comparison to mitoxantrone in a leukemic mouse model, Appl. Organomet Chem. 34 (2020), https://doi.org/10.1002/aoc.5369.
[40] N. Abbasi, H. Ghaneialvar, R. Moradi, M.M. Zangeneh, A. Zangeneh, Formulation and characterization of a novel cutaneous wound healing ointment by silver nanoparticles containing Citrus lemon leaf: a chemobiological study, Arab. J. Chem. 14 (2021) 103246, https://doi.org/10.1016/j.arabjc.2021.103246.
[41] M. Jung, H. Kim, J.W. Hwang, Y. Choi, M. Kang, C. Kim, J. Hong, N.K. Lee, S. Moon, J.W. Chang, S. Choi, S. Oh, H. Jang, D.L. Na, B.-S. Kim, Iron oxide nanoparticle-incorporated mesenchymal stem cells for Alzheimer's disease treatment, Nano Lett. 23 (2023) 476–490, https://doi.org/10.1021/acs.nanolett.2c03682.
[42] A. Behera, N. Sa, S.P. Pradhan, S. Swain, P.K. Sahu, Metal Nanoparticles in Alzheimer's Disease, J. Alzheimers Dis. Rep. 7 (2023) 791–810, https://doi.org/10.3233/ADR-220112.
[43] J. Koga-Batko, K. Antosz-Popiołek, H. Nowakowska, M. Błażejewska, E. M. Kowalik, J.A. Beszłej, J. Leszek, Nanoparticles as an encouraging therapeutic approach to Alzheimer's disease, Int. J. Mol. Sci. 26 (2025) 7725, https://doi.org/10.3390/ijms26167725.
[44] C.I.P. Chaparro, B.T. Simões, J.P. Borges, M.A.R.B. Castanho, P.I.P. Soares, V. Neves, A promising approach: magnetic nanosystems for Alzheimer's disease theranostics, Pharmaceutics 15 (2023) 2316, https://doi.org/10.3390/pharmaceutics15092316.
[45] Á. Gallo-Cordova, A. Espinosa, A. Serrano, L. Gutiérrez, N. Menéndez, M. del Puerto Morales, E. Mazarío, New insights into the structural analysis of maghemite and (MFe 2 O 4, M = Co, Zn) ferrite nanoparticles synthesized by a

microwave-assisted polyol process, Mater. Chem. Front 4 (2020) 3063–3073, https://doi.org/10.1039/D0QM00460J.
[46] M. Štampar, B. Breznik, M. Filipič, B. Žegura, Characterization of in vitro 3D cell model developed from human hepatocellular carcinoma (HepG2) cell line, Cells 9 (2020) 2557, https://doi.org/10.3390/cells9122557.
[47] S. Chen, Q. Wu, X. Li, D. Li, N. Mei, B. Ning, M. Puig, Z. Ren, W.H. Tolleson, L. Guo, Characterization of cytochrome P450s (CYP)-overexpressing HepG2 cells for assessing drug and chemical-induced liver toxicity, J. Environ. Sci. Health Part C. 39 (2021) 68–86, https://doi.org/10.1080/26896583.2021.1880242.
[48] V.A. Arzumanian, O.I. Kiseleva, E.V. Poverennaya, The curious case of the HepG2 cell line: 40 years of expertise, Int. J. Mol. Sci. 22 (2021) 13135, https://doi.org/10.3390/ijms222313135.
[49] M. Jinks, E.C. Davies, B.A. Boughton, S. Lodge, G.L. Maker, ^{1}H NMR spectroscopic characterisation of HepG2 cells as a model metabolic system for toxicology studies, Toxicol. Vitr. 99 (2024) 105881, https://doi.org/10.1016/j.tiv.2024.105881.
[50] M.T. Donato, L. Tolosa, M.J. Gómez-Lechón, 2015, Culture and Functional Characterization of Human Hepatoma HepG2 Cells. 2015, p. 77–93.
[51] Y. Ji, Y. Wang, X. Wang, C. Lv, Q. Zhou, G. Jiang, B. Yan, L. Chen, Beyond the promise: Exploring the complex interactions of nanoparticles within biological systems, J. Hazard Mater. 468 (2024) 133800, https://doi.org/10.1016/j.jhazmat.2024.133800.
[52] M. Štampar, S. Žabkar, M. Filipič, B. Žegura, HepG2 spheroids as a biosensor-like cell-based system for (geno)toxicity assessment, Chemosphere 291 (2022) 132805, https://doi.org/10.1016/j.chemosphere.2021.132805.
[53] Gallo-Cordova A., Nuñez N., Díaz-Ufano C., Veintemillas-Verdaguer S., Soler-Morala J., Palomares F.J., Lima E., Winkler E.L., Morales M. del P. Insights into the formation of free radicals using metal ferrite nanocatalysts (MFe 2 O 4, M = Fe, Mn, Zn, Co) prepared by a highly reproducible microwave-assisted polyol method.
[54] C. Rath, S. Anand, R.P. Das, K.K. Sahu, S.D. Kulkarni, S.K. Date, N.C. Mishra, Dependence on cation distribution of particle size, lattice parameter, and magnetic properties in nanosize Mn–Zn ferrite, J. Appl. Phys. 91 (2002) 2211–2215, https://doi.org/10.1063/1.1432474.
[55] W. Mekseriwattana, T. Thiangtrongjit, O. Reamtong, P. Wongtrakoongate, K. P. Katewongsa, Proteomic analysis reveals distinct protein corona compositions of citrate- and riboflavin-coated SPIONs, ACS Omega 7 (2022) 37589–37599, https://doi.org/10.1021/acsomega.2c04440.
[56] L. Kampen, A. Remmo, S.G. Twamley, A. Weller, A. Stach, P. Turko, N. Löwa, F. Wiekhorst, A. Ludwig, Rapid cellular uptake of citrate-coated iron oxide nanoparticles unaffected by cell-surface glycosaminoglycans, Nanoscale Adv. 6 (2024) 3825–3837, https://doi.org/10.1039/D4NA00277F.
[57] L. Wu, W. Wen, X. Wang, D. Huang, J. Cao, X. Qi, S. Shen, Ultrasmall iron oxide nanoparticles cause significant toxicity by specifically inducing acute oxidative stress to multiple organs, Part Fibre Toxicol. 19 (2022) 24, https://doi.org/10.1186/s12989-022-00465-y.
[58] H. Nosrati, M. Salehiabar, M. Fridoni, M.-A. Abdollahifar, H. Kheiri Manjili, S. Davaran, H. Danafar, New insight about biocompatibility and biodegradability of iron oxide magnetic nanoparticles: stereological and in vivo MRI monitor, Sci. Rep. 9 (2019) 7173, https://doi.org/10.1038/s41598-019-43650-4.
[59] M. Temelie, R.C. Popescu, D. Cocioaba, B.S. Vasile, D. Savu, 2018, Biocompatibility study of magnetite nanoparticle synthesized using a green method.
[60] A. Ivask, T. Titma, M. Visnapuu, H. Vija, A. Kakinen, M. Sihtmae, S. Pokhrel, L. Madler, M. Heinlaan, V. Kisand, R. Shimmo, A. Kahru, Toxicity of 11 metal oxide nanoparticles to three mammalian cell types *In V.itro*, Curr. Top. Med. Chem. 15 (2015) 1914–1929, https://doi.org/10.2174/1568026615666150506150109.
[61] F. Luo, S. Zhu, Y. Hu, K.-C. Yang, M.-S. He, B. Zhu, G.-X. Wang, F. Ling, Biocompatibility assessment of Fe3O4 nanoparticles using Saccharomyces cerevisiae as a model organism, Comp. Biochem. Physiol. Part C Toxicol. Pharmacol. 227 (2020) 108645, https://doi.org/10.1016/j.cbpc.2019.108645.
[62] R.-N. Li, X.-H. Da, X. Li, Cytotoxicity of Fe 3 O 4 Nanoparticles with Different Morphologies *In Vitro*, Nano 17 (2022), https://doi.org/10.1142/S1793292022500175.
[63] F. Shokrollahi, A. Salehzadeh, F. Kafilzadeh, M. Zaefizadeh, Cytotoxic effect of iron oxide nanoparticles functionalized with glucose and conjugated with Coumarin (Fe3O4@Glu-Coumarin NPs) on liver cancer, HepG2, cell line, Inorg. Chem. Commun. 157 (2023) 111380, https://doi.org/10.1016/j.inoche.2023.111380.
[64] H.A. Alhadlaq, M.J. Akhtar, M. Ahamed, Zinc ferrite nanoparticle-induced cytotoxicity and oxidative stress in different human cells, Cell Biosci. 5 (2015) 55, https://doi.org/10.1186/s13578-015-0046-6.
[65] N.L. Martínez-Rodríguez, S. Tavárez, Z.I. González-Sánchez, In vitro toxicity assessment of zinc and nickel ferrite nanoparticles in human erythrocytes and peripheral blood mononuclear cell, Toxicol. Vitr. 57 (2019) 54–61, https://doi.org/10.1016/j.tiv.2019.02.011.
[66] S.-W. Shin, K. Yang, M. Lee, J. Moon, A. Son, Y. Kim, S. Choi, D. Kim, C. Choi, N. Lee, H.C. Park, Manganese ferrite nanoparticles enhance the sensitivity of Hepa1-6 hepatocellular carcinoma to radiation by remodeling tumor microenvironments, Int. J. Mol. Sci. 22 (2021) 2637, https://doi.org/10.3390/ijms22052637.
[67] S.P. Singh, M. Kumari, S.I. Kumari, M.F. Rahman, M. Mahboob, P. Grover, Toxicity assessment of manganese oxide micro and nanoparticles in Wistar rats after 28 days of repeated oral exposure, J. Appl. Toxicol. 33 (2013) 1165–1179, https://doi.org/10.1002/jat.2887.
[68] L. Zhang, S. Xiao, X. Kang, T. Sun, C. Zhou, Z. Xu, M. Du, Y. Zhang, G. Wang, Y. Liu, D. Zhang, M. Gong, Metabolic conversion and removal of manganese ferrite nanoparticles in RAW264.7 cells and induced alteration of metal transporter gene expression, Int. J. Nanomed. 16 (2021) 1709–1724, https://doi.org/10.2147/IJN.S289707.
[69] R.G.D. Andrade, D. Ferreira, S.R.S. Veloso, C. Santos-Pereira, E.M.S. Castanheira, M. Côrte-Real, L.R. Rodrigues, Synthesis and cytotoxicity assessment of citrate-coated calcium and manganese ferrite nanoparticles for magnetic hyperthermia, Pharmaceutics 14 (2022) 2694, https://doi.org/10.3390/pharmaceutics14122694.
[70] P.R. Leroueil, S. Hong, A. Mecke, J.R. Baker, B.G. Orr, M.M. Banaszak Holl, Nanoparticle interaction with biological membranes: does nanotechnology present a janus face? Acc. Chem. Res. 40 (2007) 335–342, https://doi.org/10.1021/ar600012y.
[71] P.R. Leroueil, S.A. Berry, K. Duthie, G. Han, V.M. Rotello, D.Q. McNerny, Baker JRJr, B.G. Orr, M.M. Banaszak Holl, Wide varieties of cationic nanoparticles induce defects in supported lipid bilayers, Nano Lett. 8 (2008) 420–424, https://doi.org/10.1021/nl0722929.
[72] Y. Liu, Z. Zhang, Q. Zhang, G.L. Baker, R.M. Worden, Biomembrane disruption by silica-core nanoparticles: effect of surface functional group measured using a tethered bilayer lipid membrane, Biochim. Et. Biophys. Acta (BBA) Biomembr. 1838 (2014) 429–437, https://doi.org/10.1016/j.bbamem.2013.09.007.
[73] D. Wang, Z. Lin, T. Wang, Z. Yao, M. Qin, S. Zheng, W. Lu, Where does the toxicity of metal oxide nanoparticles come from: the nanoparticles, the ions, or a combination of both? J. Hazard Mater. 308 (2016) 328–334, https://doi.org/10.1016/j.jhazmat.2016.01.066.
[74] S. Attarilar, J. Yang, M. Ebrahimi, Q. Wang, J. Liu, Y. Tang, J. Yang, The toxicity phenomenon and the related occurrence in metal and metal oxide nanoparticles: a brief review from the biomedical perspective, Front Bioeng. Biotechnol. 8 (2020), https://doi.org/10.3389/fbioe.2020.00822.
[75] A. Kessler, J. Hedberg, E. Blomberg, I. Odnevall, Reactive oxygen species formed by metal and metal oxide nanoparticles in physiological media-a review of reactions of importance to nanotoxicity and proposal for categorization, Nanomaterials 12 (2022), https://doi.org/10.3390/nano12111922.
[76] E. Eruslanov, S. Kusmartsev, 2010, Identification of ROS Using Oxidized DCFDA and Flow-Cytometry. 2010, p. 57–72.
[77] R.J. Wydra, C.E. Oliver, K.W. Anderson, T.D. Dziubla, J.Z. Hilt, Accelerated generation of free radicals by iron oxide nanoparticles in the presence of an alternating magnetic field, RSC Adv. 5 (2015) 18888–18893, https://doi.org/10.1039/C4RA13564D.
[78] Z. Yang, C. Shan, J.J. Pignatello, B. Pan, Mn(II) acceleration of the picolinic acid-assisted fenton reaction: new insight into the role of manganese in homogeneous fenton AOPs, Environ. Sci. Technol. 56 (2022) 6621–6630, https://doi.org/10.1021/acs.est.1c08796.
[79] L. Bondarenko, R. Baimuratova, M. Reindl, V. Zach, A. Dzeranov, D. Pankratov, I. Osmushko, K. Kydralieva, G. Dzhardimalieva, D. Kolb, R. Prassl, M. Sterrer, S. P. Schwaminger, Designed magnetic nanoparticles for ferroptosis: release of iron ions from metal-organic frameworks modified with iron oxides, Mater. Today Chem. 42 (2024) 102332, https://doi.org/10.1016/j.mtchem.2024.102332.
[80] Parewa R.K., Yadav H., Saini A.K., Dadheech S., Scholar R. Synthesis of Zinc(II), Mercury(II), And Iron(III) Complexes, Their Characterization Techniques And Applications [Online]. www.ijcrt.org.
[81] K.A. McCall, C. Huang, C.A. Fierke, Function and Mechanism of Zinc Metalloenzymes, J. Nutr. 130 (2000) 1437S–1446S, https://doi.org/10.1093/jn/130.5.1437S.
[82] C. Hübner, H. Haase, Interactions of zinc- and redox-signaling pathways, Redox Biol. 41 (2021) 101916, https://doi.org/10.1016/j.redox.2021.101916.
[83] A. Manke, L. Wang, Y. Rojanasakul, Mechanisms of nanoparticle-induced oxidative stress and toxicity, Biomed. Res Int 2013 (2013) 1–15, https://doi.org/10.1155/2013/942916.
[84] A.V. Kozlov, S. Javadov, N. Sommer, Cellular ROS and antioxidants: physiological and pathological role, Antioxidants 13 (2024) 602, https://doi.org/10.3390/antiox13050602.
[85] K. Dudziak, M. Zapalska, A. Börner, H. Szczerba, K. Kowalczyk, M. Nowak, Analysis of wheat gene expression related to the oxidative stress response and signal transduction under short-term osmotic stress, Sci. Rep. 9 (2019) 2743, https://doi.org/10.1038/s41598-019-39154-w.
[86] T.P. Dalton, Y. Chen, S.N. Schneider, D.W. Nebert, H.G. Shertzer, Genetically altered mice to evaluate glutathione homeostasis in health and disease, Free Radic. Biol. Med 37 (2004) 1511–1526, https://doi.org/10.1016/j.freeradbiomed.2004.06.040.
[87] C. Han, M.-J. Kim, D. Ding, H.-J. Park, K. White, L. Walker, T. Gu, M. Tanokura, T. Yamasoba, P. Linser, R. Salvi, S. Someya, GSR is not essential for the maintenance of antioxidant defenses in mouse cochlea: possible role of the thioredoxin system as a functional backup for GSR, PLoS One 12 (2017) e0180817, https://doi.org/10.1371/journal.pone.0180817.
[88] E. Lubos, J. Loscalzo, D.E. Handy, Glutathione peroxidase-1 in health and disease: from molecular mechanisms to therapeutic opportunities, Antioxid. Redox Signal 15 (2011) 1957–1997, https://doi.org/10.1089/ars.2010.3586.
[89] E. Niki, Y. Yoshida, Y. Saito, N. Noguchi, Lipid peroxidation: mechanisms, inhibition, and biological effects, Biochem Biophys. Res Commun. 338 (2005) 668–676, https://doi.org/10.1016/j.bbrc.2005.08.072.
[90] R.K. Shukla, A. Badiye, K. Vajpayee, N. Kapoor, Genotoxic potential of nanoparticles: structural and functional modifications in DNA, Front Genet 12 (2021) 728250, https://doi.org/10.3389/fgene.2021.728250.

[91] A.R. Collins, The comet assay for DNA damage and repair: principles, applications, and limitations, Mol. Biotechnol. 26 (2004) 249–261, https://doi.org/10.1385/MB:26:3:249.
[92] A. Hartwig, T. Schwerdtle, Interactions by carcinogenic metal compounds with DNA repair processes: toxicological implications, Toxicol. Lett. 127 (2002) 47–54, https://doi.org/10.1016/S0378-4274(01)00482-9.
[93] I. Ghosh, A. Sadhu, Y. Moriyasu, M. Bandyopadhyay, A. Mukherjee, Manganese oxide nanoparticles induce genotoxicity and DNA hypomethylation in the moss Physcomitrella patens, Mutat. Res. Genet. Toxicol. Environ. Mutagen. 842 (2019) 146–157, https://doi.org/10.1016/j.mrgentox.2018.12.006.
[94] S. Alarifi, D. Ali, S. Alkahtani, Oxidative Stress-Induced DNA Damage by Manganese Dioxide Nanoparticles in Human Neuronal Cells, Biomed. Res Int 2017 (2017) 1–10, https://doi.org/10.1155/2017/5478790.
[95] A. Déciga-Alcaraz, N.L. Delgado-Buenrostro, O. Ispanixtlahuatl-Meráz, V. Freyre-Fonseca, J.O. Flores-Flores, A. Ganem-Rondero, F. Vaca-Paniagua, M. del Pilar Ramos-Godinez, R. Morales-Barcenas, Y. Sánchez-Pérez, C.M. García-Cuéllar, Y. I. Chirino, Irreversible disruption of the cytoskeleton as induced by non-cytotoxic exposure to titanium dioxide nanoparticles in lung epithelial cells, Chem. Biol. Inter. 323 (2020) 109063, https://doi.org/10.1016/j.cbi.2020.109063.
[96] P.L. Collins, C. Purman, S.I. Porter, V. Nganga, A. Saini, K.E. Hayer, G. L. Gurewitz, B.P. Sleckman, J.J. Bednarski, C.H. Bassing, E.M. Oltz, DNA double-strand breaks induce H2Ax phosphorylation domains in a contact-dependent manner, Nat. Commun. 11 (2020) 3158, https://doi.org/10.1038/s41467-020-16926-x.
[97] W.M. Bonner, C.E. Redon, J.S. Dickey, A.J. Nakamura, O.A. Sedelnikova, S. Solier, Y. Pommier, γH2AX and cancer, Nat. Rev. Cancer 8 (2008) 957–967, https://doi.org/10.1038/nrc2523.
[98] C. Crosio, G.M. Fimia, R. Loury, M. Kimura, Y. Okano, H. Zhou, S. Sen, C.D. Allis, P. Sassone-Corsi, Mitotic Phosphorylation of Histone H3: Spatio-Temporal Regulation by Mammalian Aurora Kinases, Mol. Cell Biol. 22 (2002) 874–885, https://doi.org/10.1128/MCB.22.3.874-885.2002.
[99] C. Prigent, S. Dimitrov, Phosphorylation of serine 10 in histone H3, what for? J. Cell Sci. 116 (2003) 3677–3685, https://doi.org/10.1242/jcs.00735.
[100] M. Guérard, M. Baum, A. Bitsch, G. Eisenbrand, A. Elhajouji, B. Epe, M. Habermeyer, B. Kaina, H.J. Martus, S. Pfuhler, C. Schmitz, A. Sutter, A. D. Thomas, C. Ziemann, R. Froetschl, Assessment of mechanisms driving non-linear dose–response relationships in genotoxicity testing, Mutat. Res. Rev. Mutat. Res. 763 (2015) 181–201, https://doi.org/10.1016/j.mrrev.2014.11.001.
[101] R. Corvi, F. Madia, In vitro genotoxicity testing–Can the performance be enhanced? Food Chem. Toxicol. 106 (2017) 600–608, https://doi.org/10.1016/j.fct.2016.08.024.
[102] D.P. Guimaraes, P. Hainaut, TP53: a key gene in human cancer, Biochimie 84 (2002) 83–93, https://doi.org/10.1016/S0300-9084(01)01356-6.
[103] H.E. Marei, A. Althani, N. Afifi, A. Hasan, T. Caceci, G. Pozzoli, A. Morrione, A. Giordano, C. Cenciarelli, p53 signaling in cancer progression and therapy, Cancer Cell Int. 21 (2021) 703, https://doi.org/10.1186/s12935-021-02396-8.
[104] T. Brummer, R. Zeiser, The role of the MDM2/p53 axis in antitumor immune responses, Blood 143 (2024) 2701–2709, https://doi.org/10.1182/blood.2023020731.
[105] GADD45A growth arrest and DNA damage inducible alpha [Homo sapiens (human)] - Gene - NCBI [Online]. [date unknown]. ⟨https://www.ncbi.nlm.nih.gov/gene/1647⟩.
[106] K.S. Alnajjar, J.B. Sweasy, A new perspective on oxidation of DNA repair proteins and cancer, DNA Repair 76 (2019) 60–69, https://doi.org/10.1016/j.dnarep.2019.02.006.
[107] M. Piechaczyk, R. Farràs, Regulation and function of JunB in cell proliferation, Biochem Soc. Trans. 36 (2008) 864–867, https://doi.org/10.1042/BST0360864.
[108] G.S. Jimenez, S.H. Khan, J.M. Stommel, G.M. Wahl, p53 regulation by post-translational modification and nuclear retention in response to diverse stresses, Oncogene 18 (1999) 7656–7665, https://doi.org/10.1038/sj.onc.1203013.
[109] M. Wade, Y.V. Wang, G.M. Wahl, The p53 orchestra: Mdm2 and Mdmx set the tone, Trends Cell Biol. 20 (2010) 299–309, https://doi.org/10.1016/j.tcb.2010.01.009.
[110] A. Basu, S. Haldar, 1998, The relationship between Bcl2, Bax and p53: consequences for cell cycle progression and cell death.